Acta Materialia 317 (2026) 122543

Contents lists available at ScienceDirect

Acta Materialia

journal homepage: www.elsevier.com/locate/actamat

Full length article

Ni diffusion in the equiatomic CoFeMnNiV high-entropy alloy: Unexpected impact of second-phase precipitation on bulk diffusion rates

Aditya Burla [a,*], Aditya Srinivasan Tirunilai [b], Mathias Redondo Garcia [b], G. Mohan Muralikrishna [c,*], Vladimir A. Esin [d], Daniel Schliephake [e,f], Alexander Kauffmann [b], Gerhard Wilde [a], Guillaume Laplanche [b], Sergiy V. Divinski [a,*]

[a] Institute of Materials Physics, University of Münster, 48149 Münster, Germany
[b] Institute für Werkstoffe, Ruhr-Universität Bochum, Universitätsstr. 150, D-44780 Bochum, Germany
[c] Department of Metallurgical and Materials Engineering, Indian Institute of Technology Patna, Bihta, 801106, India
[d] Institute Jean Lamour, Université de Lorraine, 54011 Nancy, France
[e] Karlsruhe Nano Micro Facility (KNMFi), Karlsruhe Institute of Technology (KIT), Hermann-von-Helmholtz-Platz 1 76344 Eggenstein-Leopoldshafen, Germany
[f] Institute for Applied Materials (IAM-WK), Karlsruhe Institute of Technology (KIT), Engelbert-Arnold-Str. 4 76131 Karlsruhe, Germany

ARTICLE INFO

Keywords:
Dual-phase high-entropy alloys
Sigma phase
Diffusion
Grain boundary diffusion
Vacancy over-saturation

ABSTRACT

Ni diffusion in the equiatomic CoFeMnNiV high-entropy alloy is measured over an extended temperature range that covers both single-phase (face-centered cubic, FCC, solid solution) as well as two-phase (FCC solid solution + σ-phase) states. In addition, Ni diffusion experiments were performed on a single-phase σ-alloy. The σ-phase precipitation is found to affect significantly the self-diffusion kinetics in the FCC solid solution. The measured tracer diffusion coefficients follow an Arrhenius-type relationship when estimated in the single-phase solid solution, and a characteristic enhancement of the Ni diffusivity is observed at lower temperatures when the σ-phase precipitates during the diffusion annealing treatments. The enhancement is significantly suppressed when the alloy is pre-aged to approach a nearly equilibrium σ-phase volume fraction at a given temperature. Since Ni volume diffusion in the σ-phase was found to be similar to that in the FCC equiatomic counterpart, the observed diffusion enhancement is attributed to an excess vacancy concentration, generated during the growth of σ-precipitates. This excess gets eliminated when approaching thermodynamic equilibrium, i.e., when precipitation ends. A simple model of the diffusion enhancement during precipitation is proposed.

1. Introduction

The dawn of the 21st century saw the development of a new class of materials known as high-entropy alloys (HEAs) or single-phase (solid solution) subsets of multi-principal element alloys [1,2]. This class of alloys originates from a novel alloying strategy, which explores the central regions of multi-dimensional phase diagrams utilizing five and more elements alloyed in equiatomic or near-equiatomic compositions. Because of the vast compositional space available, this alloying strategy offers a huge potential for developing novel alloys, often with superior properties [3].

The equiatomic CoCrFeMnNi alloy (known as Cantor alloy) and its derivatives were widely studied for their exceptional mechanical properties, especially at cryogenic temperatures [4–6]. Initially, it was believed that the Cantor alloy is a single-phase face-centered cubic (FCC) alloy, which led to a considerable amount of research [4,7–9]. Later, it was documented that secondary phases form below about 1073 K [10]. For example, annealing at 973 K for 500 days was shown to result in micrometer-large precipitates of a topologically close-packed (TCP) sigma (σ)-phase at grain boundaries [11]. This phase is known to precipitate in many engineering materials such as steels (Fe-based), superalloys (Ni and Co-based), and HEAs, during service at elevated temperatures [12]. The σ-phase typically strengthens these alloys [13], but also leads to embrittlement, depletion of strengthening elements in the matrix and crack formation, all of which are detrimental to the performance of these alloys [14–17].

By studying single-phase FCC and equiatomic subsets of the Cantor alloy, Wu et al. [18,19] showed that alloys with higher Cr concentrations were stronger, suggesting that Cr is a potential solid solution strengthener in FCC solid solutions of the Co–Cr–Mn–Fe–Ni system. Given that V has an even larger atomic radius than Cr [20], some of the present authors hypothesized and demonstrated in a previous

* Corresponding authors.
E-mail addresses: aditya.burla@uni-muenster.de (A. Burla), mohan@iitp.ac.in (G. Mohan Muralikrishna), divin@uni-muenster.de (S. Divinski).

https://doi.org/10.1016/j.actamat.2026.122543
Received 30 March 2026; Received in revised form 15 June 2026; Accepted 10 July 2026
Available online 16 July 2026

work [21] that substituting Cr with V in CoCrFeMnNi to form CoFeMnNiV would result in superior solid solution strengthening. While this was experimentally confirmed, CoFeMnNiV was unexpectedly found to have a more advantageous strength/ductility combination than CoCrFeMnNi [21]. Regarding phase stability, both V and Cr are σ-phase stabilizers [11,21,22], with V having a stronger effect, i.e., the σ-phase solvus temperatures are around 1338 K [23] and 1073 K [10,11] in the CoFeMnNiV and CoCrFeMnNi alloys, respectively. Correspondingly, the σ-phase precipitation kinetics is significantly enhanced in CoFeMnNiV with precipitates seen after annealing at 1273 K for 1 h [21]. One may ask whether atomic diffusion in CoFeMnNiV is different with respect to that in, e.g., CoCrFeMnNi if both would be evaluated at the same temperatures and whether it can be considered as "sluggish" as it is often anticipated [24].

Diffusion in HEAs was already extensively investigated [25–29] and it was originally claimed by Tsai et al. [30] that diffusion in HEAs is sluggish. However, recent studies have shown that, while diffusion is indeed sluggish in some face-centered cubic (FCC) HEA systems, this statement cannot be generalized to all of them. In this context, Dash et al. [31] suggested a correlation between the degree of lattice distortions and diffusion kinetics in HEAs, i.e., sluggish diffusion is only observed in HEAs with small lattice distortions. In hexagonal close-packed (HCP) HEAs with significant lattice distortions, tremendous diffusion enhancement (termed as "anti-sluggish" diffusion) was measured [32]. In body-centered cubic (BCC) HEAs with relatively large lattice distortions, volume diffusion was not found to be "sluggish" [33,34].

As mentioned previously, substituting Cr with V is expected to result in higher lattice distortion as V has a larger atomic radius than Cr. It is thus worth to extend the existing tracer diffusion investigations to a further FCC system with increased lattice distortion. Therefore, the first aim of this paper is to investigate the diffusion kinetics in single-phase (FCC solid solution) CoFeMnNiV HEA at high temperatures. Furthermore, the influence of σ-phase precipitation on the diffusion kinetics in CoFeMnNiV, which is prominent at temperatures below 1300 K [21], is evaluated. Simultaneously, a strong contribution of short-circuit diffusion, presumably of grain- or FCC/σ interphase boundary diffusion is observed and carefully evaluated. The study is accompanied by measurements of Ni diffusion in a bulk σ-phase alloy which are crucial for a reliable analysis of the diffusion behavior in a two-phase (FCC solid solution + σ) mixture and a robust evaluation of the short-circuit diffusion contribution.

2. Experimental procedure

2.1. Processing and annealing of the equiatomic CoFeMnNiV alloy

The equiatomic CoFeMnNiV HEA was produced by vacuum induction melting and subsequently homogenized at 1473 K for 48 h. The cast rod, which initially had a diameter of 40 mm, was mechanically deformed by rotary swaging in several steps to reduce its diameter by 60% to 17 mm. For further details concerning the alloy processing, please refer to Ref. [35]. The deformed rod was first machined on a lathe to 8 mm in diameter and then subjected to recrystallization annealing at 1353 K for 30 min. This state is henceforth referred to as the recrystallized condition (HT-0), which is initially single-phase FCC with a mean grain size of ~60 μm [21], excluding annealing twin boundaries.

Discs with a thickness of 1.2 mm and a diameter of 8 mm were cut by spark erosion for diffusion experiments. They were wrapped in a Ta foil, encapsulated in quartz ampules in an Ar atmosphere (5N purity), and subjected to a pre-diffusion heat treatment at 1173 K and 1073 K for 360 h. These states are further referred to as heat-treated I (HT-I) and heat-treated II (HT-II) conditions, respectively, which are two-phase FCC+σ with σ-area fractions of 0.19 for HT-I and 0.27 for HT-II (Table 1). The equilibrium composition of the σ phase was determined by SEM-EDS point analyses in the two-phase FCC+σ alloys (HT-I and HT-II). The approximate composition $Co_{20}Fe_{21}Mn_{18}Ni_{12}V_{29}$ (in at.%) was found not to vary significantly with annealing temperature.

Table 1
Heat-treated states and corresponding σ-phase area fractions prior to tracer diffusion experiments.

State	Annealing temperature (K)	Annealing time (h)	σ-phase fraction
Recrystallized (HT-0)	–	0	0
Heat treated I (HT-I)	1173	360	0.19
Heat treated II (HT-II)	1073	360	0.27

2.2. Synthesis of a bulk σ-phase alloy

For comparative tracer diffusion measurements, a bulk σ-phase alloy was prepared. To this end, the average composition of the nearly equilibrium σ-precipitates was rounded to the nearest whole numbers, and 1 at.% V was added at the expense of Ni to ensure that the composition falls in the single-phase region of the phase diagram. This resulted in a nominal composition $Co_{20}Fe_{21}Mn_{18}Ni_{11}V_{30}$ in at.%, for which pieces of pure metals (V, Mn, Fe, Co, and Ni, all with a purity better than 99.7 wt.%) were weighed appropriately. In the case of Mn, flakes were etched in a 10:1 diluted solution of nitric acid, to prevent formation of a new oxide layer prior to melting, thereby limiting the amount of oxide inclusions in the alloy. For the other metals, etching was unnecessary.

Pieces of the constituent elements were placed in the chamber of an AM/0.5 arc-melting device (Edmund Bühler GmbH), which was pumped to a pressure of $5 \cdot 10^{-2}$ mbar and flooded with Ar. This process was repeated three times, followed by a high vacuum pumping stage to achieve a pressure of less than $5 \cdot 10^{-5}$ mbar. The chamber was then flooded with Ar to a pressure of 600 mbar. Before melting, a small piece of Zr was melted to getter any residual oxygen in the chamber. The elements were then melted in a concave Cu mold to obtain a button after solidification. The button was flipped and remelted five times before it was finally melted and cast into a cuboidal Cu mold of dimensions $50 \times 27 \times 23$ mm^3. The solidified button was cooled down slowly by progressively reducing the arc current. Still, the button cracked during final cooling to room temperature. However, this was inconsequential to subsequent characterization experiments, see below, for which a specimen was cut from one of the halves. This piece was taken from a region that was in contact with the Cu mold and experienced the fastest cooling rate.

2.3. Characterization

Sample surfaces were prepared by mechanical and chemical polishing to a mirror-like finish. Phase analyses of the $Co_{20}Fe_{20}Mn_{20}Ni_{20}V_{20}$ and $Co_{20}Fe_{21}Mn_{18}Ni_{11}V_{30}$ alloys were performed by X-ray diffraction (Siemens D5000) using Cu Kα radiation (λ = 0.154 nm). The X-ray diffraction (XRD) patterns were measured in the Bragg Brentano geometry for the 2θ interval from 30° to 100° with a step size of 0.02° and a dwell time of 20 s.

Backscattered electron (BSE) imaging and electron backscatter diffraction (EBSD) were performed with a Jeol-7200F scanning electron microscope (SEM), while energy dispersive X-ray spectroscopy (EDS) was carried out with an FEI Nova NanoSEM 230R SEM.

Differential thermal analyses (Setaram Labsys TG-DSC) were performed in high-purity Ar atmosphere, using a heating rate of 30 K/min, to study phase transformations in the $Co_{20}Fe_{20}Mn_{20}Ni_{20}V_{20}$ alloy in different heat-treated conditions (HT-0, HT-I and HT-II) as well as for the as-cast $Co_{20}Fe_{21}Mn_{18}Ni_{11}V_{30}$ bulk σ-phase alloy.

Table 2
Temperature T and time t of the radiotracer diffusion experiments and determined diffusion coefficients D_v of ^{63}Ni. Some samples were heat-treated for the diffusion experiments at the specified temperatures T_{ht} for the times t_{ht}. The states HT-0, HT-I, and HT-II are defined in Table 1. For completeness, the determined parameters of short-circuit diffusion, α, β, and $P = s \cdot \delta \cdot D_{gb}$, are listed as well. Here α and β are determined by Eqs. (2) and (3), respectively, and the so-called triple product P is defined as the product of the segregation factor s, interface width δ, and the interface diffusion coefficient D_{gb}.

State	Heat-treatment		Diffusion annealing		D_v	α	β	$P = s \cdot \delta \cdot D_{gb}$
	T_{ht}	t_{ht}	T	t	m^2/s	s		m^3/s
	K	10^4 s	K	10^4 s				
HT-0	–	–	1423	2.16	$6.62^{+0.44}_{-0.45} \times 10^{-15}$	2.09×10^{-5}	0.88	$1.40^{+0.10}_{-0.11} \times 10^{-19}$
			1363	5.76	$3.28^{+0.16}_{-0.17} \times 10^{-15}$	1.82×10^{-5}	1.00	$9.03^{+0.50}_{-0.51} \times 10^{-20}$
			1273	8.64	$3.09^{+0.77}_{-0.78} \times 10^{-16}$	4.86×10^{-5}	3.63	$1.15^{+0.16}_{-0.17} \times 10^{-20}$
			1173	26.64	$7.65^{+0.21}_{-0.37} \times 10^{-17}$	5.54×10^{-5}	5.81	$4.01^{+0.15}_{-0.29} \times 10^{-21}$
			1173	10.8	$1.50^{+0.50}_{-0.29} \times 10^{-16}$	1.97×10^{-4}	14.15	$5.40^{+0.85}_{-0.52} \times 10^{-21}$
			1073	60.48	$1.35^{+0.13}_{-0.11} \times 10^{-17}$	8.75×10^{-5}	10.33	$7.97^{+0.38}_{-0.29} \times 10^{-22}$
			1073	3.6	$2.76^{+0.21}_{-0.10} \times 10^{-17}$	2.51×10^{-4}	29.63	$1.63^{+0.10}_{-0.10} \times 10^{-21}$
			1073	0.36	–	1.32×10^{-3}	271.27	$1.03^{+0.10}_{-0.10} \times 10^{-21}$
HT-I	1173	129.6	1173	26.64	$4.56^{+0.67}_{-0.26} \times 10^{-17}$	7.17×10^{-5}	7.16	$2.27^{+0.11}_{-0.21} \times 10^{-21}$
			1073	60.48	$8.15^{+0.10}_{-1.4} \times 10^{-18}$	1.13×10^{-4}	12.17	$5.44^{+0.10}_{-0.52} \times 10^{-22}$
HT-II	1073	129.6	1073	60.48	$1.91^{+0.42}_{-0.10} \times 10^{-17}$	7.35×10^{-5}	13.23	$8.83^{+1.05}_{-0.39} \times 10^{-22}$

2.4. Radiotracer technique

The samples were metallographically prepared to obtain a smooth and mirror-like surface. The ^{63}Ni radioactive isotope (68 keV β-decays, half-life of about 100 years) was available as a HCl solution, which was highly diluted to achieve a specific radioactivity of about 5 kBq/µl. About 10 kBq of the diluted ^{63}Ni tracer was deposited on the samples and dried under a sodium vapor lamp. The samples were wrapped in Ta foils, sealed in quartz tubes in an Ar atmosphere, and subjected to various diffusion annealing treatments, as listed in Table 2.

After diffusion annealing treatments, the samples were radially reduced by about 1 mm to eliminate potential effects of surface and/or lateral diffusion. The samples were then sectioned using a precision mechanical plane-parallel grinder. The section thickness was determined by the weight loss of the samples after each grinding step using a high-precision microbalance (with an accuracy of ±0.1 µg for the average section weights of 1 mg or more). A liquid scintillation counter (TRI CARB 2910TR) was used to measure the radioactivity of each section. The measured penetration profiles correspond to relative specific radioactivity (background corrected) divided by the section mass, which is proportional to the tracer concentration in the section, $\bar{C}(x)$, plotted against the diffusion depth, x.

2.5. Secondary ion mass spectroscopy

The bulk σ-phase ingot was cut into small pieces (approximately 5 mm × 5 mm × 2 mm) by spark erosion and one face was polished to a mirror-like finish. A non-radioactive highly-enriched ^{64}Ni isotope (natural abundance of about 0.93%) was used. A layer of ^{64}Ni with an average thickness of 85 nm was deposited in a physical vapor deposition (PVD) device applying vacuum better than 10^{-5} mbar. The samples were then sealed in quartz ampules in a 5N high purity Ar atmosphere and were subjected to diffusion annealing at 1173 K for 3 h, 1073 K for 1 h, and 973 K for 20 h. The annealing temperatures and times were selected after a few trial-and-error experiments based on the tracer diffusivities measured by the radiotracer technique in the CoFeMnNiV alloy while keeping the intended diffusion length under 2 µm to obtain reliable data.

Ni diffusion was measured for the brittle bulk σ-phase alloy using a time-of-flight secondary ion mass spectroscopy (ToF-SIMS V, IONTOF GmbH). The ToF-SIMS measurements were performed over a 250 × 250 µm^2 area in dual beam mode with a Cs^+ (2 keV) sputter beam and a primary beam of Bi^+ (25 keV) for the chemical characterization of the crater. The resulting crater depth was measured using a profilometer (Sensofar PLμ Neox). To produce reliable volume diffusion coefficients, the region of interest was chosen to exclude any microstructure defects such as grain boundaries or cracks. A sample in the as-deposited state (no diffusion annealing) was also probed to establish a reference state.

3. Results

3.1. Characterization

3.1.1. X-ray diffraction of the single-phase and dual-phase alloys

The XRD analyses (see Fig. 1) revealed that the as-recrystallized alloy (HT-0) is single-phase FCC (space group Fm$\bar{3}$m, Strukturbericht designation A1), the bulk σ-alloy shows a single-phase tetragonal crystal structure ($P4_2/mnm$, $D8_b$), while the HT-I and HT-II conditions are two-phase, as evidenced by the presence of diffraction peaks belonging to the σ- and FCC phases. The lattice parameters of the two phases were obtained from Rietveld refinement, and the associated uncertainties, estimated as ±0.001 nm, indicate the quality of the fit. The FCC-phase lattice parameter remained essentially similar across all three conditions, with $a = 0.3610$ nm for HT-0, $a = 0.3609$ nm for HT-I, and $a = 0.3608$ nm for HT-II. A minor decrease of the lattice parameter of the FCC phase correlates with progressive V depletion in the matrix due to the σ-phase precipitation.

The σ-phase has lattice parameters of $a = 0.8843$ nm, $c = 0.4588$ nm and $a = 0.8838$ nm, $c = 0.4587$ nm for HT-I and HT-II, respectively, while those of the bulk σ-phase alloy are $a = 0.8845$ nm, $c = 0.4585$ nm. These minute variations in the lattice parameters also correlate with small variations of the composition, especially of the V content .

3.1.2. Microstructural and chemical characterization

The microstructure and distribution of elements in the CoFeMnNiV alloy after different heat treatments were studied by SEM and SEM-EDS, respectively, as shown in Fig. 2. Here, we only show the Ni and V EDS elemental maps because they show the strongest partitioning to the FCC-matrix and σ-precipitates, respectively. For the sake of completeness, the elemental EDS maps of Co, Fe, and Mn are shown in the Supplementary Material, Fig. S1. In the HT-0 state, the microstructure reveals a homogeneous distribution of the alloying elements in the matrix and the presence of a few oxides enriched in Mn and V, Figs. 2(a) and S1. These non-coherent oxides should not affect radiotracer diffusion measurements, as their volume fraction is below 0.3% by area [23]. In the HT-I state, Fig. 2(b) reveals a dual-phase microstructure with a Ni-rich (V-depleted) FCC matrix and V-rich (Ni-depleted)

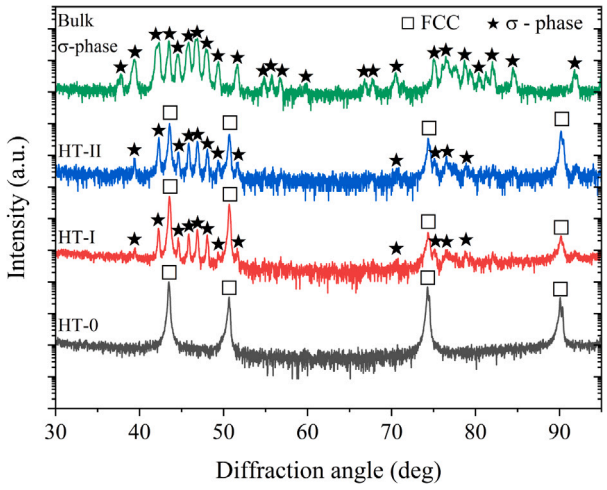

Fig. 1. XRD patterns (using a log scale) of the CoFeMnNiV alloy in HT-0 (single-phase FCC), HT-I and HT-II (two-phase FCC+σ) conditions and that of the bulk σ-phase alloy. The indexed XRD peaks are marked.

Table 3
Compositions (in at.%) of different phases measured by SEM-EDS in the equiatomic CoFeMnNiV and bulk σ-phase alloys. The data were averaged over more than 10 different positions within the given phases. The uncertainties associated with EDS are about ±0.5 at.%. Standard deviations were found to be below this threshold except for the σ-phase in the HT-II state (±1.5 at.% for Ni and V), due to the fact that the information volume is very close to the size of the σ-precipitates.

Sample	Phase(s)	Composition (at.%)				
		Co	Fe	Mn	Ni	V
HT-0	FCC	19.7	20.2	20.0	20.0	20.1
HT-I	Matrix (FCC)	20.0	20.4	20.2	21.2	18.2
	+19% σ phase	19.6	21.5	18.2	12.3	28.4
HT-II	Matrix (FCC)	20.6	20.3	20.6	20.7	17.8
	+27% σ phase	20.1	21.3	18.5	12.4	27.7
bulk σ	σ-phase	19.9	20.9	18.0	10.8	30.4

σ-precipitates. These precipitates exhibit a coarse morphology and are mostly present along grain boundaries with a few precipitates within grains. In contrast, the dual-phase microstructure is much finer in the HT-II condition with a much higher number density of σ-precipitates, Fig. 2(c). The compositions (in at.%) of the FCC and σ-phases for the HT-0, HT-I, and HT-II conditions, which were determined by EDS point analyses, are given in Table 3.

The inverse pole figure (IPF) map in Fig. 3(a) reveals that the HT-0 state of CoFeMnNiV is single-phase FCC without a dominant texture. The average grain size is ~60 μm with several annealing twins (twin boundaries were excluded when evaluating the grain size). The twin density is rather low. These results are in good agreement with our previous work [23], in which we showed that, on average, there is one annealing twin boundary for every three grains. These features persist in the FCC matrix after prolonged annealing at 1173 K and 1073 K, i.e., grain growth did not occur in the HT-I and HT-II states as evidenced in Figs. 4 and 5. Rounded σ-allotriomorphs with different crystallographic orientations were observed to form along grain boundaries. Figs. 3(b2) and (c2) show that portions of grain boundaries are completely covered by chains of σ-allotriomorphs that grew into each other. Furthermore, thin disc-shaped precipitates have also formed within grains. Note that the precipitates are discs in 3D that appear as needles on 2D cross sections [12].

The microstructural evolutions during isothermal aging at 1173 and 1073 K are shown in Figs. 4 and 5, respectively. At both temperatures, the σ-phase area fraction increases over time. After 3 h (Fig. 4(a)), the σ-phase precipitated almost exclusively at grain boundaries, whereas longer annealing (74 h, Fig. 4(b)) led to σ-phase precipitation within grains. Prolonged annealing for 360 h resulted in the formation of a quasi-continuous film of σ-phase along FCC grain boundaries with a few coarse σ-discs within grains. This corresponds to the microstructure (Fig. 4(c)) of the HT-I condition prior to radiotracer diffusion.

After annealing at 1073 K for 10 h (Fig. 5(a)), σ-allotriomorphs precipitated along grain boundaries. Additionally, many fine, submicrometer, disc-shaped σ-precipitates are visible within grains. With increasing annealing time to 168 h (Fig. 5(b)), the disc-shaped σ-precipitates lengthened and impinged on each other to form an interconnected network. After 360 h (Fig. 5(c)), the network has slightly coarsened, i.e., the discs have become slightly thicker. This latter microstructure was selected as the starting condition for the radiotracer experiments corresponding to the HT-II state. The precipitation kinetics have been investigated in a separate study, and the detailed results will be reported elsewhere. At 1173 K, precipitation was found to start (1% completion) already after annealing for 20 min, the transformation is half completed after 40 h and precipitation ends (99%) after 300 h of annealing. At 1073 K, the precipitation kinetics are slower. It begins after 30 min, a half completion is reached after 50 h, and precipitation ends after approximately 360 h. The diffusion times were chosen to comply with the precipitation kinetics.

3.1.3. *Microstructural and chemical characterization of the bulk σ-phase alloy*

The microstructure, crystallography, and chemical homogeneity of the as-cast σ-phase alloy were characterized using BSE imaging, EBSD and EDS analyses. The overview BSE image in Fig. 6(a) reveals the presence of grains with different shades of gray, dark submicron particles and long cracks, indicating that the alloy is intrinsically brittle [36,37]. From the same region, an EBSD phase map was recorded and shown with a forward scatter detector (FSD) overlay in Fig. 6(b). Here, the black, red, and light blue pixels correspond to locations from which the Kikuchi patterns were unindexed, indexed as σ-phase, and indexed as FCC phase, respectively. In Fig. 6(b), more than 99% of the scanned area was indexed as the σ-phase, indicating that the regions with different shades of gray in Fig. 6(a) correspond to grains and subgrains of the σ-phase with different crystallographic orientations.

An EDS area analysis of a large region with dimensions 60 × 48 μm^2 yielded a composition of $Co_{20}Fe_{21}Mn_{18}Ni_{11}V_{30}$ (see Table 3), which is in excellent agreement with the targeted one. A region of interest, which is marked with a yellow frame in Figs. 6(a) and (b), is magnified in Figs. 6(c1) and (c2), respectively. The high-resolution BSE image in Fig. 6(c1) shows that black and dark gray particles are embedded into the σ-phase matrix. To identify the nature of these secondary phases, EBSD and EDS analyses were carried out on the same region, see Figs. 6(c2,d,e) and (f), respectively. In Fig. 6(c2), the small blue particles were indexed as FCC-phase, while the matrix was indexed as σ-phase. Representative Kikuchi patterns of the σ and FCC-phases are shown in Figs. 6(d) and (e), respectively. The EDS elemental maps in Fig. 6(f) show a homogeneous elemental distribution within the σ-phase, while the FCC-phase is relatively enriched in Ni and correspondingly depleted in V. In the oxygen-elemental map in Fig. 6(f), the black particles in Figs. 6(a) and (c1) are found to be enriched in oxygen, suggesting that these are oxides.

In summary, the $Co_{20}Fe_{21}Mn_{18}Ni_{11}V_{30}$ alloy consists mainly of σ-phase, which is chemically homogeneous, and the minor phases are oxides and FCC particles, which are highlighted in Fig. 6(c1) with green and light blue arrows, respectively.

3.1.4. *Differential thermal analyses*

Complete results of DTA analyses are shown in Fig. S2, Supplementary Material. In Fig. 7, the relevant temperature interval between 1300 K and 1650 K is highlighted. For the equiatomic CoFeMnNiV alloy in the HT-0, HT-I, and HT-II states, the endothermic peak at ~1550 K

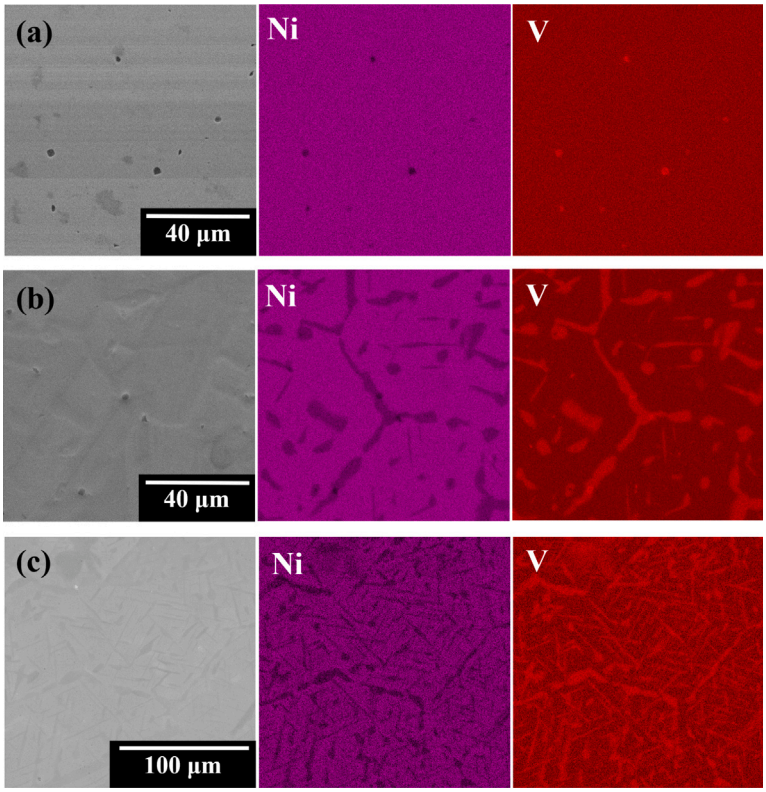

Fig. 2. EDS elemental maps of Ni and V in the CoFeMnNiV alloy: (a) HT-0 condition showing a homogeneous FCC matrix with dispersed oxide particles; (b) HT-I condition, highlighting the presence of V-rich σ-phase along grain boundaries and within the FCC matrix; (c) HT-II condition, showing a pronounced presence of the V-rich σ-phase along grain boundaries and within the FCC matrix.

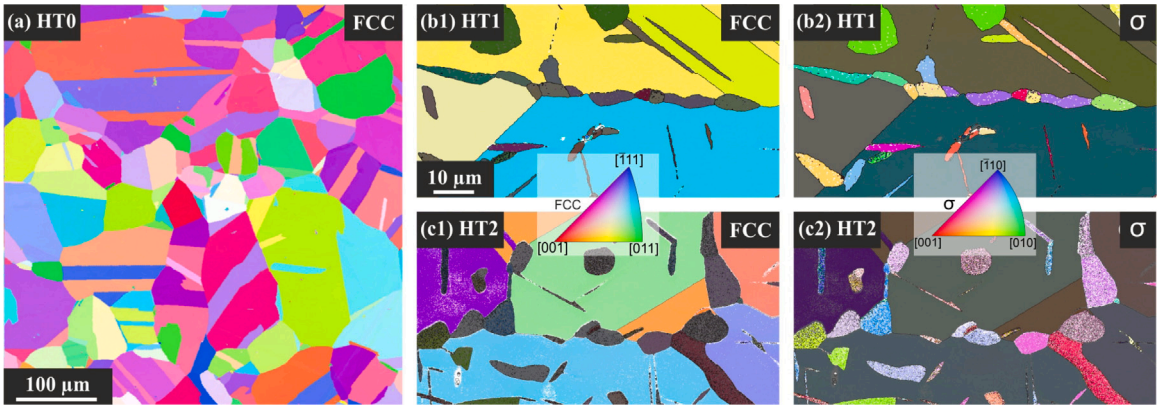

Fig. 3. EBSD grain orientation maps of the equiatomic CoFeMnNiV alloy in the single-phase HT-0 state (a), two-phase HT-I condition (b1,b2), and two-phase HT-II state (c1,c2). The phase content in the microstructures is listed in Table 1. The grain orientations of the FCC phase are shown in (a,b1,c1), while those of the σ-phase are displayed in (b2,c2). The corresponding color keys are indicated in stereographic triangles.

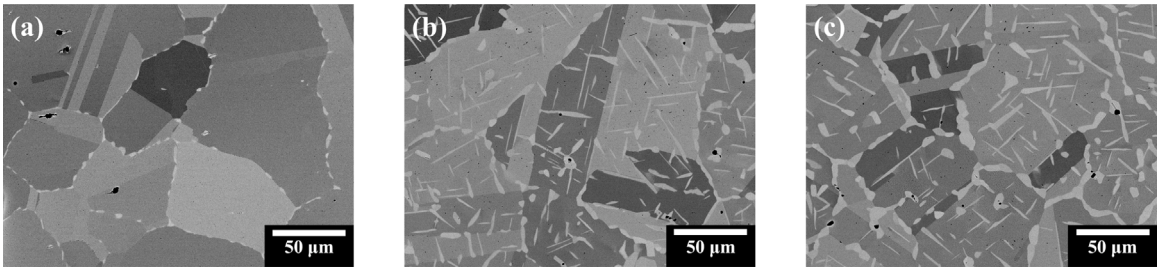

Fig. 4. SEM-BSE micrographs (atomic number and orientation contrast) illustrating the σ-phase precipitation during isothermal aging at 1173 K. BSE images of the CoFeMnNiV alloy after annealing for 3 h (a), 74 h (b), and 360 h (c).

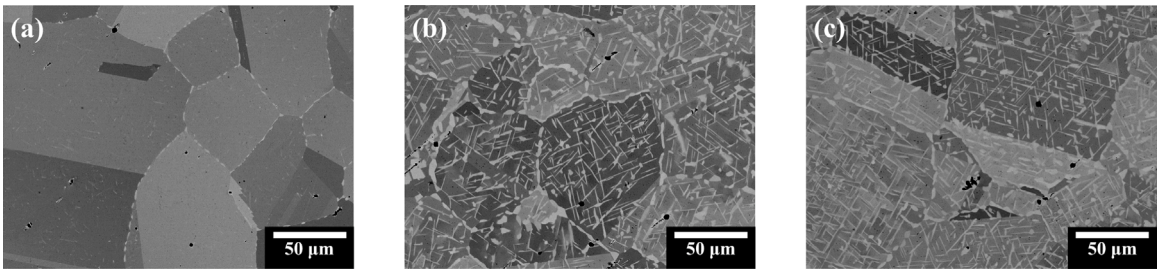

Fig. 5. SEM-BSE micrographs (atomic number and orientation contrast) illustrating the microstructural evolution during annealing at 1073 K for 10 h (a), 168 h (b), and 360 h (c) at 1073 K. The BSE images reveal the formation of bright, V-enriched σ-precipitates in a dark FCC matrix.

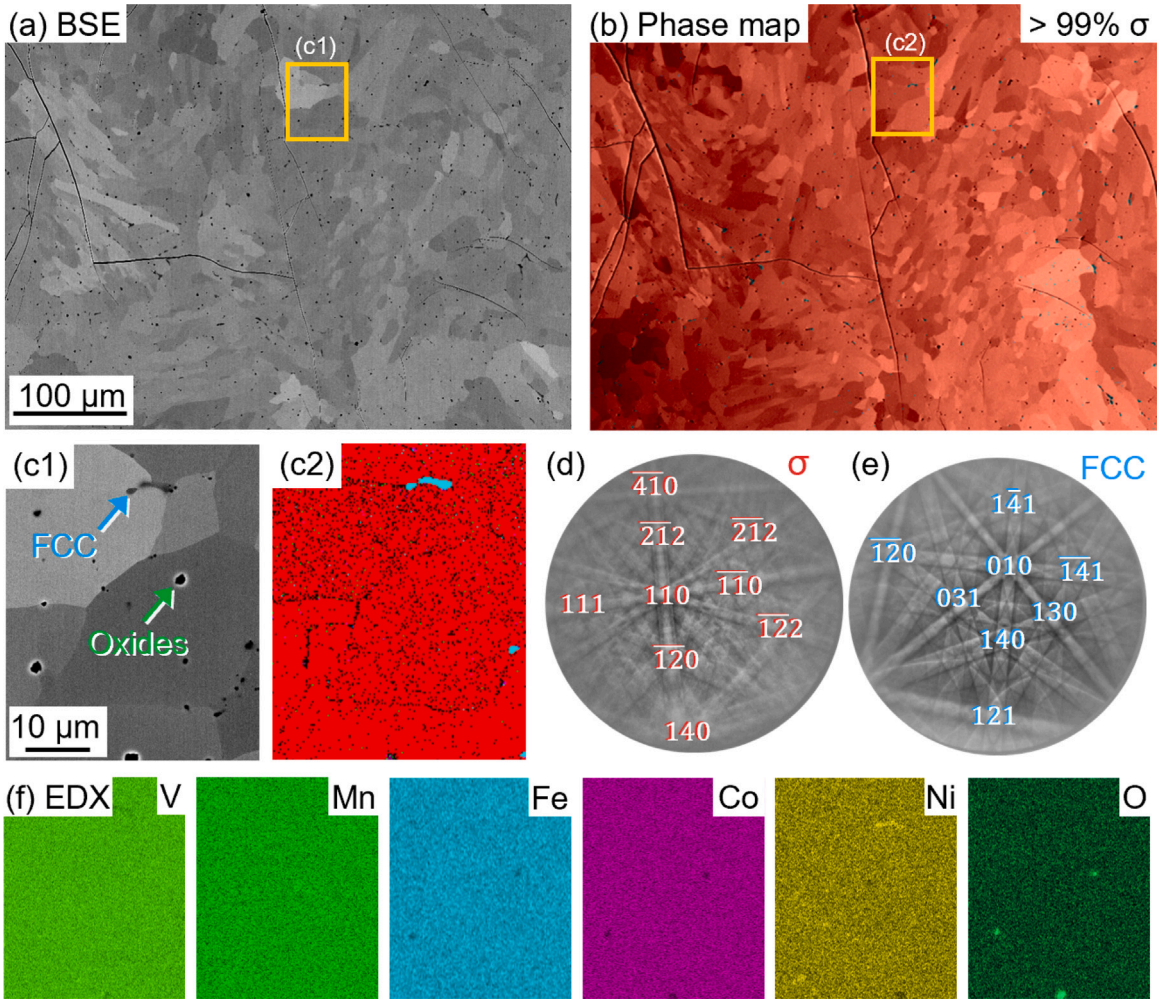

Fig. 6. Microstructure of the σ-phase alloy in the as-cast state. (a) BSE overview showing a polycrystalline microstructure with several cracks. (b) EBSD phase map with an FSD overlay where σ and FCC phases appear red and blue, respectively. The yellow-framed region in (a) is magnified in (c1), where minor phases can clearly be distinguished. An EBSD phase map from the same region in (c2) reveals the presence of blue FCC particles. Representative Kikuchi patterns of the (d) σ-phase matrix and (e) FCC particles. (f) EDS elemental maps of V, Mn, Fe, Co, Ni, and O showing that the oxides and FCC precipitates are O and Ni-rich, respectively. (For interpretation of the references to color in this figure legend, the reader is referred to the web version of this article.)

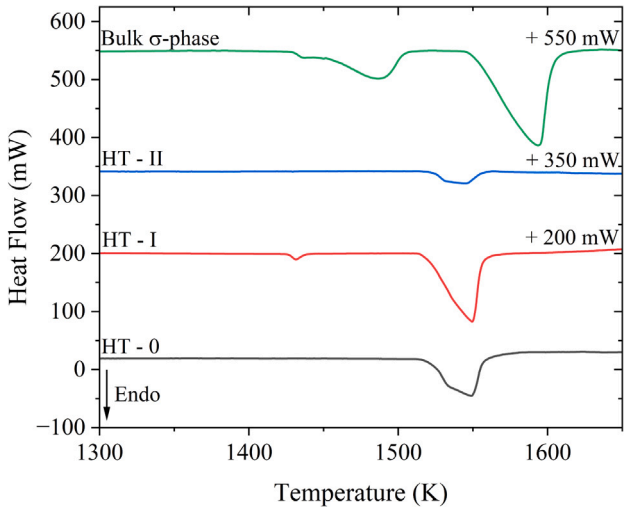

Fig. 7. Heat flow curves for the bulk σ-phase, HT-0, HT-I, and HT-II conditions measured by DTA at a heating rate of 30 K/min.

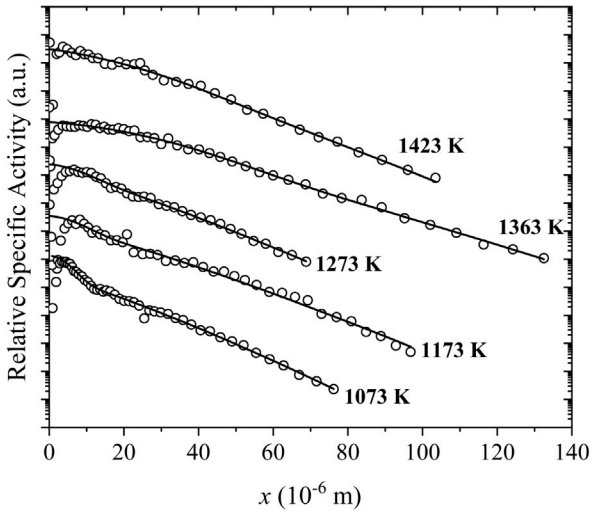

Fig. 8. Penetration profiles for ^{63}Ni diffusion in the initially single-phase FCC equiatomic CoFeMnNiV alloy (HT-0 state). The solid lines correspond to fits after Eq. (1). Due to a potential tracer evaporation and artificial grinding-in effects, the analysis does not include near-surface points at depths of less than several micrometers.

corresponds to melting. In contrast, the bulk σ-phase alloy exhibits two endothermic peaks at ~1490 K and ~1590 K. While the second peak corresponds to melting, a careful study of binary phase diagrams from the Co–Fe–Mn–Ni–V system indicates that the first peak corresponds to a σ-to-BCC phase transformation. However, further work is required to fully confirm this.

3.2. Diffusion measurements

The measured penetration profiles for ^{63}Ni diffusion in the initially single-phase FCC equiatomic CoFeMnNiV alloy (HT-0 state) are shown in Fig. 8 as $\ln \bar{C}$-vs.-x plots. Here, $\bar{C}(x)$ is the layer tracer concentration, which is proportional to the measured relative specific activity, and x is the penetration depth. The profiles determined at 1273 K, 1173 K and 1073 K clearly reveal two distinct contributions (diffusion branches), e.g., there is a kink in the penetration profile obtained at 1073 K at x = 10 μm, Fig. 8. In contrast, this feature is less apparent in the profiles measured at 1423 K and 1363 K.[1] At first glance, the transition from a two-branch to an apparent single-branch profile as temperature increases from 1273 K to 1363 K correlates with the solvus temperature of the σ-phase, i.e., the alloy is two-phase FCC+σ below 1338 K [23], and single-phase FCC at higher temperatures. However, the appearance of a second diffusion branch, extending down to about 100 μm in Fig. 8, might also indicate a significant contribution of short-circuit diffusion processes such as grain boundary (GB) diffusion, interphase boundary diffusion, and pipe diffusion, whose contributions are known to increase relative to bulk diffusion with decreasing temperature [38]. Therefore, a dedicated analysis is required to clarify this aspect, which will be presented in Section 4.4.

Having inspected the initial microstructure in the HT-0 state, Fig. 3(a), we can conclude that the first branch, especially at elevated temperatures (≥ 1273 K), corresponds to direct volume diffusion in the FCC matrix (average grain size: ~60 μm).[2] At temperatures above 1273 K, these are general high-angle grain boundaries (GBs) in the FCC matrix. At lower temperatures and with increasing diffusion time, the FCC GBs become increasingly decorated with σ-precipitates, Figs. 3(b2) and (c2), and interphase boundaries, i.e., the FCC/σ interfaces might additionally contribute to the short-circuit diffusion transport.

The present penetration profiles are analyzed using a formal GB-diffusion model [39], and subsequent analysis will justify the correctness of this approximation. The analysis of the GB diffusion problem in a polycrystalline material depends crucially on the given kinetic regime. After Harrison [40], the present measurements are performed in the so-called B-type kinetic regime. In this case, a tracer atom diffuses fast along GBs with a following leakage to the crystalline volume and a final random walk within the grains at slower rates. According to the results of Le Claire's analysis [41] of the exact solution by Suzuoka [42] of the corresponding GB diffusion problem, the logarithm of the tracer concentration due to GB diffusion decays with the depth raised to the power of 6/5$^{\text{th}}$. The total tracer concentration due to a combination of bulk and GB diffusion is approximated by,

$$\bar{C}(x) = A \exp\left(-\frac{x^2}{4D_v t}\right) + B \exp\left[-\left(\frac{x}{L_{gb}}\right)^{6/5}\right], \quad (1)$$

with A and B being the fitting parameters. Here, the relative depth of GB diffusion, L_{gb}, is related to the GB diffusivity, i.e., the triple product $P = s \cdot \delta \cdot D_{gb}$ [43], where s, δ, and D_{gb} are the segregation factor, the GB width, and the GB diffusion coefficient, respectively. The validity of the B-type kinetics conditions and the exact expression for L_{gb} depends on the values of the parameters α,

$$\alpha = \frac{s\delta}{2\sqrt{D_v t}}, \quad (2)$$

and β,

$$\beta = \frac{P}{2D_v\sqrt{D_v t}}. \quad (3)$$

The B-type kinetics regime holds if $\alpha < 0.1$ and $L_{gb}^2 = \frac{P}{1.308}\sqrt{\frac{t}{D_v}}$ for $\beta > 10^4$ [43]. For $\beta < 2$, i.e., at the two highest temperatures, see Table 2, Eq. (1) is not suitable [43] and the exact Suzuoka solution [42] was used. In the present work, the segregation factor for GB self-diffusion, i.e., the ratio of Ni concentration within the interface to that in the bulk near a GB, is close to unity, $s \approx 1$.

[1] The second branch is hardly visible at these high temperatures due to small values of the GB diffusion parameter β, $\beta < 1$, as discussed in Section 4.4.

[2] Volume diffusion in the σ-phase as a second branch would correspond to a characteristic Gaussian-type contributions, i.e. $-\ln \bar{C} \propto x^2$, in contrast to the observed ~linear shape of the deeper branches in Fig. 8. However, a contribution of volume diffusion within the σ-grains to the first branches cannot be excluded at this stage, see Section 3.2.2.

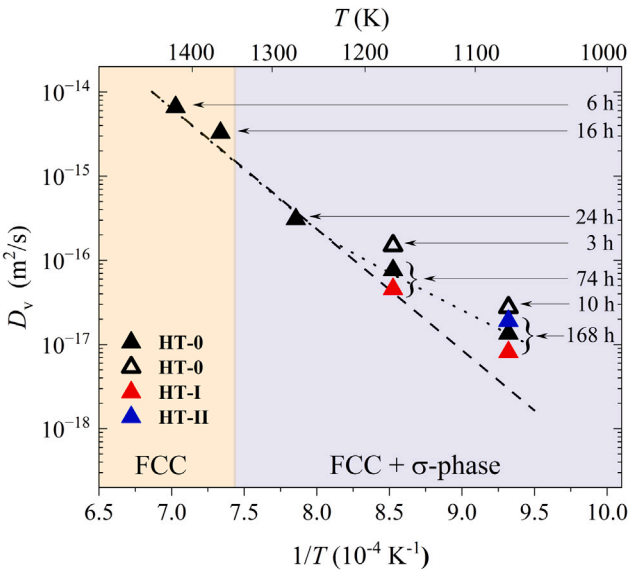

Fig. 9. Ni bulk diffusion coefficients, D_v, in the CoFeMnNiV alloy in HT-0 (black triangles), HT-I (red triangles) and HT-II (blue triangle) states as function of the inverse absolute temperature $1/T$. The shorter diffusion annealing treatments at 1173 K and 1073 K for the initial HT-0 state are represented by black open triangles. The measured diffusion coefficients in the HT-0 state, filled black triangles, reveal an upward trend in the corresponding Arrhenius-type dependence below 1273 K, dotted line. An extrapolation of the high-temperature data is indicated by a dashed line. The temperature intervals corresponding to single-phase (FCC solid solution) and two-phase (FCC+σ) equilibria are indicated with yellow and blue backgrounds, respectively. The statistical uncertainties of single measurements are within the symbol size if not explicitly shown. The diffusion times are specified indicating an exhaustion of the relative diffusion enhancement observed at lower temperatures. (For interpretation of the references to color in this figure legend, the reader is referred to the web version of this article.)

A remark is due here. In this formal analysis, we assumed a combination of bulk and GB diffusion. Due to the σ-phase precipitation, a certain contribution of interphase boundary diffusion, i.e., diffusion along the FCC/σ boundaries, might be expected too, see Section 4.4. The corresponding analysis depends strongly on the bulk diffusivities in the FCC and σ-phases [43], which have to be evaluated. The general structure of Eq. (1) holds, but modifications of the expressions for the diffusion parameters might be required, especially for the effective length of interphase boundary diffusion. For simplicity, these corrections will be discussed below, together with the estimation of the σ-phase contribution to the diffusion behavior. Fortunately, as the analysis will demonstrate, the adopted simplifications do not affect the derived data in a significant manner.

3.2.1. Volume diffusion in the CoFeMnNiV alloy

Eq. (1) (or the exact Suzuoka solution at the two highest temperatures) was used to fit the penetration profiles in Fig. 8 and the volume diffusion coefficients of Ni were determined, Table 2. The D_v values evaluated for the HT-0 state are drawn as filled black triangles in the D_v-vs.-$1/T$ plot shown in Fig. 9 (adopting a logarithmic scale for the diffusion coefficients). An upward curvature in the Arrhenius-type coordinates is obvious, indicated by the dotted line in Fig. 9). This tendency is schematically visualized by drawing a linear Arrhenius-type approximation of the three highest data points and its extrapolation to lower temperatures, dashed line in Fig. 9.

This behavior advocates a relative enhancement of the Ni diffusion rate at lower temperatures within the two-phase temperature range with respect to the single-phase high-temperature data. To elucidate the reasons for the volume diffusion enhancement at 1173 K and 1073 K in CoFeMnNiV, dedicated time-dependent diffusion measurements were performed, see Fig. 10.

In particular, two types of experiments were performed at 1173 K, see the penetration profiles in Fig. 10(a):

(i) the initially single-phase FCC microstructure (0% of σ, HT-0 state), which is metastable at 1173 K, was annealed for 3 and 74 h, during which the σ-phase particles precipitated and grew;
(ii) the initially two-phase (19% of σ) microstructure (HT-I state), corresponding to the equilibrium state at 1173 K, was further diffusion-annealed for 74 h.

At 1073 K, the following diffusion measurements were performed, see the concentration profiles in Fig. 10(b):

(i) the initially single-phase FCC microstructure (0% of σ, HT-0 state), which is metastable at 1073 K, was annealed for 1, 10, and 168 h;
(ii) the initially two-phase (27% of σ) microstructure (HT-II state), corresponding to the equilibrium state at 1073 K, was diffusion-annealed for 168 h;
(iii) the initially two-phase (19% of σ) microstructure (HT-I state) was diffusion-annealed for 168 h. During this experiment, the microstructure is slightly unstable, and the σ-phase area fraction is expected to increase from 19 % to 27%.

These diffusion experiments were designed to capture the atomic transport with and without the concomitant precipitation of the σ-phase at different stages of the precipitation.

The penetration profiles, shown in Fig. 10, again reveal a two-branch character and they were fitted using Eq. (1). The results are summarized in Table 2 and shown in Fig. 9. In order to highlight the diffusion time-dependence of the determined volume diffusion coefficients, they are shown in Fig. 11 as functions of the initial state and the annealing time.

At 1173 K, the volume diffusion coefficient determined in the HT-0 state is found to decrease with increasing diffusion time from 3 h to 74 h. It is even lower if diffusion is measured in the equilibrated microstructure (HT-I state), see Fig. 11. In other words, the diffusion enhancement associated with σ-phase precipitation gradually decreases, compare the open and filled black triangles in Fig. 9, and vanishes in the HT-I state, in which precipitation was complete before diffusion annealing. In fact, the corresponding tracer diffusion coefficient, red triangle in Fig. 9, agrees well with the high-temperature Arrhenius dependence, dashed line.

At 1073 K, the diffusion behavior is qualitatively similar, i.e., the diffusion coefficient decreases with increasing diffusion time in the state HT-0, compare open and filled black triangles in Fig. 9. The prolonged pre-annealing at 1173 K (HT-I state) also decreases the measured bulk diffusion coefficient at 1073 K (red triangle, HT-II state). A prolonged pre-annealing treatment at 1073 K (blue triangle in Fig. 11) slightly reduces the tracer diffusion coefficient at 1073 K with respect to the diffusion rate measured for the HT-0 state applying a short annealing time (open black triangle). However, the value is similar (even slightly higher) than that measured in the HT-0 state applying a long annealing time (filled black triangle). All values measured at 1073 K exceed the diffusion rate corresponding to the extrapolation of the high-temperature diffusion data shown by a black dashed line in Fig. 9 or as blue dashed line in Fig. 11.

3.2.2. Diffusion in the bulk σ-phase alloy

Since the σ-phase appears in the CoFeMnNiV alloy at low temperatures, diffusion in it has to be evaluated independently for a further analysis. The successfully synthesized bulk σ-phase allows such diffusion experiments. However, the conventional radiotracer diffusion method cannot be applied to the bulk σ-phase due to the presence of multiple cracks in the alloy, which would provoke artifacts and

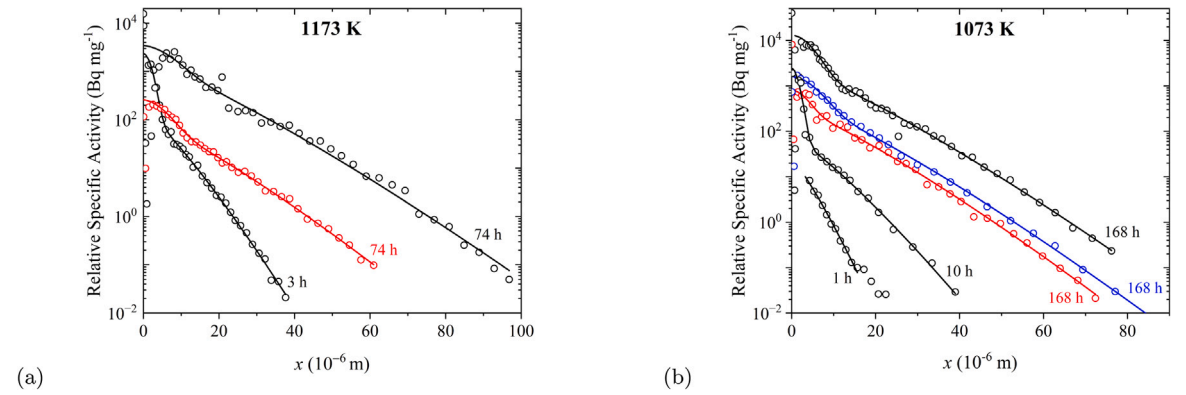

Fig. 10. Penetration profiles of ^{63}Ni tracer diffusion measured at 1173 K (a) and at 1073 K (b) for different diffusion times in HT-0 (single-phase FCC, black), HT-I (FCC+19% σ, red) and HT-II (FCC+ 27% σ, blue) conditions and the corresponding fit after Eq. (1). (For interpretation of the references to color in this figure legend, the reader is referred to the web version of this article.)

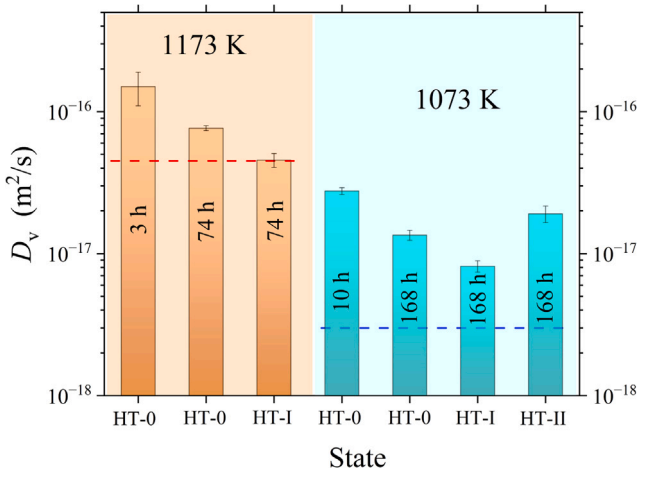

Fig. 11. Tracer diffusion coefficients measured at 1173 and 1073 K using different diffusion times (indicated) and varying the initial state. The dashed lines correspond to the tracer diffusion coefficients estimated by an extrapolation of the high-temperature data, the dashed line in Fig. 9. The error bars indicate the estimated accuracies of the measured diffusion coefficients.

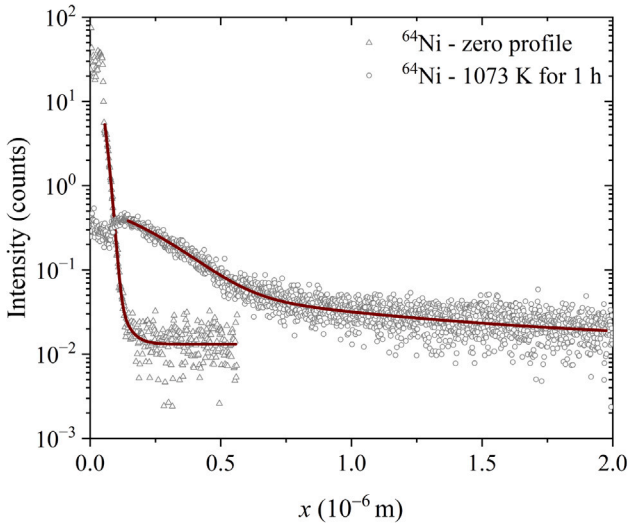

Fig. 12. Depth distribution of the relative intensity, ^{64}Ni/^{58}Ni, measured with ToF-SIMS, showing the as-deposited layer (zero-profile, triangles) and the diffusion profile obtained after annealing at 1073 K for 1 h in the bulk σ-phase (circles). The solid lines represent the corresponding fits after Eq. (4).

falsify the results of any layer-averaging method. We utilized a ToF-SIMS analysis in order to circumvent this problem. However, it is worth noting that the accessible tracer penetration depths, i.e., $\sqrt{D_v t}$, are limited to a few hundreds nanometers in the depth-profiling mode. This implicitly imposes limitations on the temperature window of the corresponding diffusion measurements, since reasonable diffusion times range from a fraction of an hour to several weeks. As a result, the diffusion measurements in the σ-phase were conducted at temperatures below 1200 K.

A Ni grain, highly-enriched (> 95%) with the ^{64}Ni isotope, was evaporated on top of the bulk σ-phase sample, whose microstructure is shown in Fig. 6. After suitable annealing treatments, see Table 4, depth distributions of Ni were analyzed using ToF-SIMS. As an example, the depth distributions of the ^{64}Ni isotope for the as-deposited and diffusion-annealed (1073 K for 1 h) states are shown in Fig. 12. The penetration profiles measured at 1173 K and at 973 K are shown in Supplementary Material, Fig. S4. Crack-free areas were carefully selected for all such measurements. In order to account for potential irregularities during sputtering, the ^{64}Ni signal was normalized on that of the main Ni isotope, ^{58}Ni, and the ratio ^{64}Ni/^{58}Ni was plotted.

Table 4
Temperature T and time t of the ^{64}Ni tracer diffusion experiments in the bulk σ-phase alloy and the determined diffusion coefficients D_v.

T	t	D_v
K	h	m^2/s
1173	3	$4.3^{+1.0}_{-2.0} \times 10^{-17}$
1073	1	$7.7^{+1.3}_{-1.4} \times 10^{-18}$
973	20	$1.27^{+0.26}_{-0.25} \times 10^{-18}$

The SIMS profiles were approximated using the following expression,

$$\bar{C} = a_0 \operatorname{erfc}\left(\frac{x - x_0}{\sigma}\right) + a_1 \exp\left(-\frac{x}{\gamma}\right) + a_{bcg}\,, \tag{4}$$

with a_0, σ, a_1, γ, and a_{bcg} being the fit parameters. a_{bcg} corresponds to the residual concentration of the ^{64}Ni isotope in the alloy (due to the presence of about 0.9% of ^{64}Ni in natural Ni) normalized on that of ^{58}Ni (about 68% in natural Ni), which determines the background value of the SIMS signal. The first term in Eq. (4) (complementary error function) approximates the distribution of the deposited isotope (including its diffusion-induced broadening) and the second one (the

exponentially decaying function) corresponds to a profile distortion due to the sputtering-induced effects, e.g., see Ref. [44]. The parameter σ in the erfc function (the first term in Eq. (4)) was determined in the as-deposited ($\sigma = \sigma_0$) and diffusion-annealed ($\sigma = \sigma_1$) states, and the volume diffusion coefficients were estimated from the relation $\sigma_1^2 = \sigma_0^2 + 4D_v t$.

The determined volume diffusion coefficients of ^{64}Ni in the bulk σ-phase alloy are listed in Table 4 and shown in Fig. 13(a). A direct comparison of the bulk diffusion data in Tables 2 and 4 as well as Fig. 13(a) suggests that the Ni diffusion rates measured by the ToF-SIMS analysis for the bulk σ-phase and by the radiotracer technique for the single-phase FCC and two-phase FCC+σ alloys are at least within the same order of magnitude. Within this comparison, the isotope effect [45] due to the usage of the ^{63}Ni and ^{64}Ni isotopes can safely be neglected, since the required corrections are below $f_{64}(\sqrt{m_{64}/m_{63}} - 1)$ [45], and thus below 1%. Here, f_{64} is the correlation factor for vacancy-mediated diffusion of the ^{64}Ni isotope and m_{64} and m_{63} are the masses of the ^{64}Ni and ^{63}Ni isotopes, respectively.

4. Discussion

4.1. Justification of the correctness of our previous analyses to estimate bulk diffusivities in the FCC phase

The measured bulk diffusion coefficients in the two-phase FCC+σ states in Table 2 are, in fact, weighted averages of the corresponding volume diffusion coefficients in the FCC and σ-phases. Depending on the microstructure, diffusion time, and the partitioning factors, the simple model proposed by Hart [46] or a more elaborated, e.g., Maxwell–Garnett approach [47] might be used to correlate the measured effective diffusion coefficients with the diffusivities in the constituent phases, e.g., see the analyses by Kalnin et al. [48] or by Li et al. [49]. These analyses were simplified by assuming stationary, not evolving two-phase microstructures. In the present study, the fraction of the σ-phase evolves during the course of the diffusion experiments, even changing the connectivity of the different phases, which demands a more sophisticated consideration. Since the diffusion coefficients determined in the CoFeMnNiV alloy and in the bulk σ-phase alloy are similar within the same order of magnitude (e.g., at 1073 K in Fig. 13(a)), the required corrections to the reported bulk diffusion coefficients in the disordered FCC solid solutions can be estimated to vary from about −50% (if the Ni diffusion rate in the σ-phase would significantly be enhanced with respect to that in the FCC phase) to +20% (if the diffusion rate in the σ-phase would be frozen).[3] Based on the results shown in Fig. 13(a), the lower-bond uncertainty, i.e., −50%, can be significantly decreased. Indeed, the Ni diffusion coefficient in the σ-phase hardly exceeds that in the FCC solid solution at 1173 K, since the measured diffusion rate in the two-phase mixture was found to decrease with increasing diffusion time (and simultaneously increasing the σ-phase fraction). Therefore, the uncertainty in the Ni diffusion data can be estimated as ±15%, which is typical for the radiotracer diffusion method [50]. More importantly, the bulk diffusion data in Table 2 represent very reasonable approximations of the Ni diffusion rates in the FCC solid solution.

The similar rates of Ni bulk diffusion in the CoFeMnNiV alloy and the bulk σ-phase resemble the behavior reported for the CoCrFeMnNi Cantor alloy and the corresponding Cr-rich σ-phase [51], as indicated by the corresponding Arrhenius curves that are represented by green and red lines in Fig. 13(a), respectively. To differentiate the two σ-phases, we will refer to the former as σ(V-based) and the latter as σ(Cr-based). These σ-phases feature the same crystallographic structure but differ in chemical composition, and likely, in site occupancies of their respective sublattices [37].

The similar values of the diffusion coefficients in the FCC and σ phases correlate with similar packing densities of the two lattices. Note that the radiotracer diffusion measurements in the $AlCoCrFeNiTi_{0.2}$ compositionally complex alloy substantiated significantly lower diffusion rates in the corresponding σ-phase with respect those on the constituting BCC (in fact B2-ordered) phase [49].

4.2. Temperature dependence of Ni bulk diffusion in the FCC solid solution

The Arrhenius diagram in Fig. 9 shows a clear distinction between the high- and low-temperature diffusion behaviors in the CoFeMnNiV HEA in its HT-0 state. At high temperatures, where the alloy is single-phase FCC, the diffusion coefficients follow a well-defined Arrhenius relationship. This indicates that atomic transport in this regime is governed by equilibrium point-defect concentrations and by a single thermally activated diffusion mechanism. In contrast, at lower temperatures, especially at 1173 K and 1073 K, where precipitation of the σ-phase becomes pronounced, see Figs. 4 and 5, the measured diffusion coefficients, see filled black triangles in Fig. 9, are significantly enhanced relative to the Arrhenius extrapolation of the high-temperature data, which is represented by a dashed line.

To shed light on this intriguing behavior, time-dependent diffusion measurements at low temperatures were performed. Experiments conducted at 1173 K in the HT-I state with an equilibrated microstructure, yielded diffusion coefficients that are consistent with the high-temperature Arrhenius extrapolation, red triangle in Fig. 9. However, measurements in the HT-0 state, where the σ-phase particles evolve during the diffusion experiment, exhibit systematically enhanced diffusion rates with respect to the high-temperature extrapolation (open black triangle) potentially due to an excess vacancy concentration. These observations indicate that the transient enhancement of diffusion at 1173 K is associated with ongoing σ-phase precipitation, whereas in an equilibrated microstructure the vacancy concentration corresponds to the thermal equilibrium.

The time-dependent diffusion measurements at 1073 K reveal distinct behaviors across the different heat treated states (Fig. 11). The measurements in the HT-0 state, performed for different annealing times, show that the determined volume diffusion coefficients in the FCC phase remain approximately similar, varying by about a factor of two at most for the diffusion times used. The measurement in the HT-I condition yielded the lowest diffusion rate. Interestingly, in the HT-II state, i.e., under equilibrated conditions, the diffusivity is relatively enhanced with respect to that value and is closer to the diffusivities measured in HT-0 state.

In Fig. 13(a), the expected temperature dependence of the near-equilibrium bulk Ni diffusivity in the FCC CoFeMnNiV solid solution is represented by a black line that was fitted to four experimental data points, i.e., the three data points measured above 1200 K in the HT-0 state and the 1173-K data point determined in the HT-I state. We argue that these data points represent intrinsic, near-equilibrium diffusion properties of Ni in the FCC solid solution. An Arrhenius-type approximation of these data in the temperature range of 1423 K – 1173 K is given by:

$$D_v^{Ni} = \left(2.50^{+17}_{-2.2}\right) \times 10^{-4} \times \exp\left(-\frac{(287 \pm 22)\,\mathrm{kJ/mol}}{RT}\right) \mathrm{m^2/s}\,. \quad (5)$$

At 1073 K, the measured Ni diffusion rates in FCC CoFeMnNiV (determined in both HT-I and HT-II states) exceed the predictions according to Eq. (5) by a factor of three to ten (Fig. 9). The dispersion of the data is larger than the typical uncertainty of bulk diffusion, estimated at ±15% [50]. Therefore, it is safe to conclude that there is

[3] The upper-bond estimates can be derived from a very crude approximation of the measured effective diffusion coefficient D_{eff} in a stable two-phase microstructure as $D_{eff} = (1 - f)D_{FCC} + f D_\sigma$ after Hart [46]. Here f is the volume fraction of the σ phase.

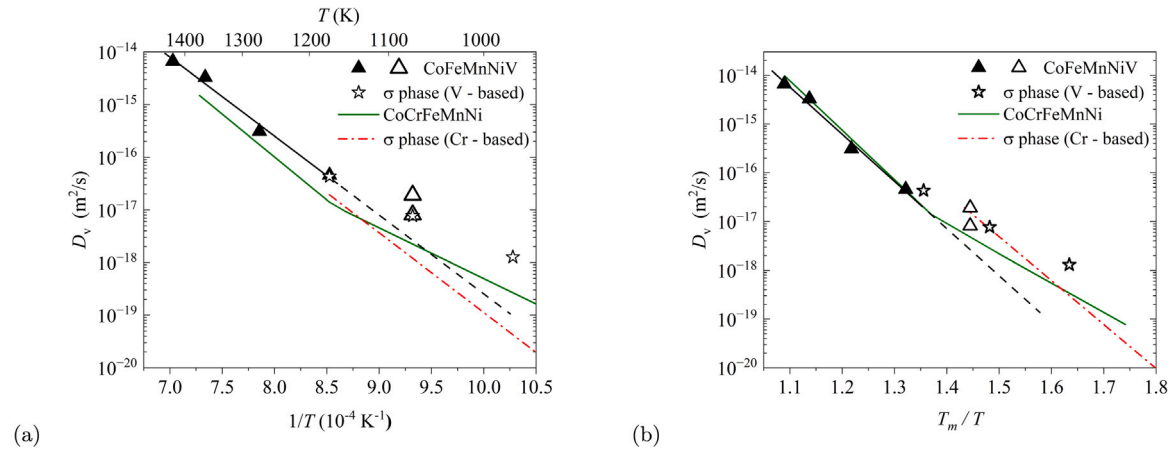

Fig. 13. Ni volume diffusion in the equiatomic CoFeMnNiV alloy (at 1173 K and 1073 K, only measurements corresponding to (pre-aged) fully precipitated microstructures were considered) and in the $Co_{20}Fe_{21}Mn_{18}Ni_{11}V_{30}$ σ-phase as a function of (a) the inverse, $1/T$, and (b) inverse homologous, T_m/T, temperatures. Here, T_m is the solidus temperature of the corresponding alloy. In (a), the diffusion data for the σ(V-based) alloy (stars) almost coincide with the measured Ni diffusion coefficients in the CoFeMnNiV HEA (black triangles, with the open triangles representing measurements at 1073 K). For comparison, the Ni volume diffusion rates determined in the CoCrFeMnNi alloy and its σ(Cr-based)-phase counterpart are shown with green solid and red dashed–dotted lines, respectively. The black dashed line corresponds to the Arrhenius-type extrapolation of the temperature dependence established at higher temperatures (black solid line). . (For interpretation of the references to color in this figure legend, the reader is referred to the web version of this article.)

a kink in the Arrhenius dependence of Ni bulk diffusion in CoFeMnNiV at about 1173 K.

In Fig. 13, the Ni diffusion rates measured in the present CoFeMnNiV alloy at presumably near-equilibrium conditions are compared to those reported in the literature for Ni diffusion in the equiatomic CoCrFeMnNi alloy [25,52] with respect to the inverse absolute temperature, $1/T$, and the inverse homologous temperature, T_m/T, scales. Here, T_m is the solidus temperature of the corresponding compound, determined by DTA in Fig. 7. Several features are noteworthy:

- At the same absolute temperatures in their single-phase state (FCC solid solution), i.e., above ~1338 K for CoFeMnNiV and above ~1073 K for CoCrFeMnNi [22], the Ni diffusion rate in CoFeMnNiV exceeds that in CoCrFeMnNi by a factor of two to three at 1423 K and 1363 K. In the two-phase region for CoFeMnNiV, this enhancement is slightly larger, but of a similar magnitude within the accuracy of the tracer diffusion measurements. The enhanced diffusion rates in CoFeMnNiV with respect to those in CoCrFeMnNi at least correlate with elevated lattice distortions in the former.
- Both CoFeMnNiV and CoCrFeMnNi feature kinks in the corresponding Arrhenius-type temperature dependencies at about 1100 K to 1150 K, Fig. 13(a). The kink is however at a slightly higher homologous temperature in CoFeMnNiV than in CoCrFeMnNi, Fig. 13(b).
- At the same absolute temperature, Ni bulk diffusion in the σ(V-based) alloy is faster than in the σ(Cr-based) one, though these diffusion rates are similar on the homologous temperature scale.

The kink might be related to a different composition of the V-depleted FCC solid solution after decomposition and/or to the appearance of short-range order in the alloy, similarly to the behavior seen in the CoCrFeMnNi alloy by Smekhova et al. [53]. These two factors might also be related.

In the Cantor alloy (CoCrFeMnNi), the kink of the green line in Fig. 13 was alternatively discussed in terms of a potential σ(Cr-based)-phase precipitation and/or short-range ordering below about 1100 K [52]. A characteristic change of dominant vacancy environments in the CoCrFeMnNi alloy below 1000 K was indeed observed using element-specific extended X-ray absorption fine structure (EXAFS) measurements [53]. In CoCrFeMnNi, a preferential Mn–vacancy binding was seen at high temperatures of 1300 K, whereas an increased concentration of Ni atoms in the nearest vicinity of the vacancies was observed at 973 K [53]. Similar measurements for the CoFeMnNiV HEA might provide further insights into a potential evolution of the short-range order, including the vacancy environment.

We conclude that the Arrhenius-type approximation of Ni diffusion in CoFeMnNiV, Eq. (5), is limited to the temperature range of 1423 K – 1173 K, and an enhancement of the Ni diffusion rates in the FCC solid solution with respect to that dependence at lower temperatures cannot be excluded even at equilibrium conditions in the CoFeMnNiV alloy with an equilibrated two-phase microstructure, i.e. without an excess vacancy concentration.

4.3. Precipitation-induced diffusion enhancement in FCC solid solution

The nucleation of disc-shaped σ-phase precipitates within the FCC solid solution is related to the fact that there is a good match between the FCC and σ-lattices at a special semi-coherent interface, i.e., when the basal {001}-plane and the $\langle 1\bar{1}0\rangle$-direction of the σ-phase are parallel to the close-packed {111}-plane and close-packed $\langle 1\bar{1}0\rangle$-direction of the FCC-phase [54], respectively. Basically the same orientation relationships are found in the present case, too, see the texture analysis in Supplementary Material, Fig. S3. During growth, the σ-discs lengthen at a much faster rate than they thicken, owing to the larger mobility of their incoherent edges compared to that of the semi-coherent broad faces [12].

The volumetric, $\Delta V/V$, and lattice misfits, ε, associated with the precipitation of σ-discs are estimated using the room-temperature lattice parameters of the FCC and σ-phases determined by XRD (see Section 3.1.1):

$$\Delta V/V = \frac{(1/30)a_\sigma^2 c_\sigma - (1/4)a_{\mathrm{FCC}}^3}{(1/4)a_{\mathrm{FCC}}^3}, \tag{6}$$

$$\varepsilon_r = \frac{a_\sigma - (\sqrt{2}/5)a_{\mathrm{FCC}}}{(\sqrt{2}/5)a_{\mathrm{FCC}}}. \tag{7}$$

and

$$\varepsilon_h = \frac{c_\sigma - (2/\sqrt{3})a_{\mathrm{FCC}}}{(2/\sqrt{3})a_{\mathrm{FCC}}}. \tag{8}$$

Here, a_σ and c_σ are the lattice parameters of the σ-phase, a_{FCC} is the lattice parameter of the FCC-matrix, ε_r and ε_h are the lattice misfits

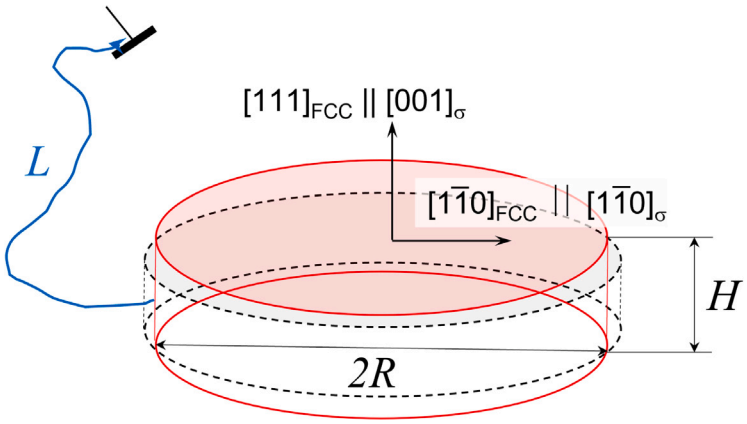

Fig. 14. Schematic presentation of the volumetric effects by disc-like σ-phase precipitation. A disc of radius $R + |\varepsilon_r|$ and thickness $H - |\varepsilon_h|$ is cut in the matrix (black dashed lines) and a σ precipitate of radius R and thickness H is inserted (red solid lines). The orientation relationship is indicated for the flat (001)-oriented facet of the σ-precipitate, which is parallel to the (111) plane of the FCC matrix [54]. As a result, there is an excess free volume in the matrix at the tip of the precipitates, which gives rise to vacancy generation. These vacancies then diffuse to sinks, e.g. to dislocations or the flat surfaces of the precipitates where the matrix is compressed. The blue line sketches a possible vacancy path of length L. (For interpretation of the references to color in this figure legend, the reader is referred to the web version of this article.)

along the $\langle 1\bar{1}0\rangle$ and $\langle 111\rangle$ directions of the FCC-phase, respectively (Fig. 14).

Although the overall formation of the σ-phase is associated with a net volumetric expansion of $\Delta V/V = 1.7 \pm 1.2$ % and that the σ-phase lattice is $\varepsilon_h = 10 \pm 1$ % larger than that of the matrix along the $[001]_\sigma$ direction of the σ-discs, the lattice of the σ-phase along the broad semi-coherent faces of the precipitates is shorter than that of the matrix by $\varepsilon_r = -2.1 \pm 0.4$ % along the $\langle 1\bar{1}0\rangle$ direction. The exact value depends on the crystallographic direction within the (001) plane of the σ phase, though it is negative. In other words, during the FCC-to-σ transformation, a unit volume expands along the direction perpendicular to the disc-shaped precipitates (along the [001] direction of the σ-phase and [111] direction of the FCC-phase) and shrinks along the radial directions of the discs. The schematic in Fig. 14 illustrates this anisotropy of the volumetric effect due to the σ-phase formation. Disc-shaped precipitates with the diameter $2R$ and thickness H are considered, see Section 3.1.2. We are considering this anisotropy of the volumetric effect during σ-phase growth as the main factor which can lead to a vacancy concentration, $c_{Va} = c_{Va}^{eq} + c_{Va}^{ex}$, different from the equilibrium value c_{Va}^{eq}, i.e., to an excess vacancy concentration, c_{Va}^{ex}, affecting the atomic diffusion rate,

$$D^{*\prime} = \left(1 + \frac{c_{Va}^{ex}}{c_{Va}^{eq}}\right) D^*, \tag{9}$$

where D^* is the tracer diffusion coefficient corresponding to the equilibrium conditions.

We believe that the volume change due to σ-phase precipitation affects mainly the diffusion in the FCC-phase due to its more disordered state, as compared to that of σ. Therefore, diffusion in the FCC-matrix is further discussed.

Potentially, several dominant mechanisms can be suggested to explain the observed diffusion enhancement. As alternative scenarios driven by the σ-phase precipitation one may consider (i) non-equilibrium vacancy generation; (ii) short-circuit transport via transformation induced dislocations; (iii) GB or interphase boundary (IPB) contribution; (iv) changes in the chemical composition; (v) short-range ordering, or (vi) influence of mechanical stresses due to the volume change. Definitely, all these processes can be coupled and contribute to different extent to the observed behavior. Though, it is instructive to elucidate and quantify a prevalent mechanism.

It is important to highlight that not only a diffusion enhancement, but its transient, non-monotonic time dependence have to be explained.

First, the effect of hydrostatic stress induced by volume change during precipitation should be taken into account [45]. According to the analysis of the misfit presented above, the FCC-matrix is under compression at the vicinity of broad interfaces and in tension in the vicinity of edges of σ precipitates. The increased vacancy concentration can thus be expected at the edges and may lead to a diffusion enhancement. However, simple estimates indicate that a 10-fold diffusion acceleration would have required a stress of several GPa in the FCC-phase, which seems unrealistic at 1073 and 1173 K.

In principle, an apparent increase in volume diffusivity might arise from enhanced short-circuit transport via dislocation networks, grain boundaries or interphase boundaries at lower temperatures, i.e. scenarios (ii)-(iii) above. However, such a scenario has to fulfill the A-type diffusion kinetics conditions; otherwise, a distinct short-circuit contribution would be detected in the penetration profiles under the B-type kinetics. Simple geometric considerations further indicate that the grain size would need to be below ~10 μm to allow a significant overlap of the diffusion fluxes from opposite GBs, which is inconsistent with the experimentally observed average grain size exceeding 10 μm (Fig. 3). Moreover, such an effect would be expected to persist under the prolonged annealing treatment, which is not observed.

Changes in composition, scenario (iv), certainly influence the tracer diffusivities; however, the previous results on the Cantor alloy system [55,56] indicate that the variations in atomic diffusivities remain marginal for deviations within ±3% from the equiatomic composition. Furthermore, such diffusion enhancement would remain permanent after approaching equilibrium, in contrast to the transient behavior observed here. A transient enhancement of the effective diffusion coefficient with subsequent its degradation has been reported by Rickman [57], performing kinetic Monte-Carlo simulations of diffusion in a binary alloy with a strong segregation tendency of one component to linear or planar defects. Though, the enhancement was relatively small, below 20%, and it was explained by segregation-induced effective "screening" of the obstacles by fast diffusing atoms from the slower ones. The effect was seen only for intermediate defect densities [57], which correspond to the dislocation densities of about 10^{14} to 10^{15} m^{-2}, by far larger than the dislocation density in a well-annealed polycrystal. Thus, one may expect a certain impact from the segregation of V atoms at GBs on Ni diffusion, but this phenomenon cannot solely explain the observed diffusion behavior.

Short-range ordering (SRO) has also been proposed as a factor influencing diffusion in the high-entropy alloys [53,58,59]. Nevertheless, ordering is generally expected to reduce diffusivity due to increased

correlation effects on atomic jumps [60,61], and such effects would likely persist once established equilibrium is reached.

In summary, this analysis supports the scenario that the observed non-monotonic evolution of the diffusion enhancement is most likely induced by a transient variation of the vacancy concentration during the microstructural evolution, i.e. by non-equilibrium vacancy production.

Therefore, we also consider the excess vacancies generated in the FCC-phase at the incoherent edges of σ-precipitates due to a decrease in local volume as a dominant scenario. We assume that this volume deficit is compensated for by the generation of an equivalent excess volume in the form of excess vacancies. Then, the number of excess vacancies N_{Va}^{ex} produced per unit volume of the FCC-phase by N^{σ}-precipitates of the same mean volume $\overline{V^{\sigma}}$ due to a volume contraction $\overline{|\delta V^{\sigma}|}$ is,

$$N_{Va}^{ex} = N^{\sigma} \times \frac{\overline{|\delta V^{\sigma}|}}{\Omega_{Va}}, \tag{10}$$

where Ω_{Va} is the vacancy formation volume. The volume contraction is related to the mean volume as $\overline{|\delta V^{\sigma}|} = |\varepsilon_r| \times \overline{V}^{\sigma}$.

We assumed here that the nucleation stage is relatively short and corresponds to very first instances of the diffusion annealing treatment. Therefore, the precipitate total volume evolves only due to their growth, i.e., $N^{\sigma} \approx const$. Thus, at the edges, an excess free volume is continuously generated during precipitate growth that is assumed to result in vacancy emission during precipitates' lengthening. Considering that σ-precipitates are discs of radius R and thickness H (Fig. 14) and that their lengthening is much faster than their thickening ($G = \frac{dR}{dt} \gg \frac{dH}{dt}$, where G is the lengthening rate), H can be considered as almost constant during the diffusion experiment. Therefore, the mean precipitate volume, $\overline{V^{\sigma}}$, evolves as

$$\frac{d\overline{V^{\sigma}}}{dt} = 2\pi RHG. \tag{11}$$

The excess vacancy concentration (in at.%) is

$$c_{Va}^{ex} = N_{Va}^{ex} V_m / N_A = \Omega N_{Va}^{ex}, \tag{12}$$

where N_A is the Avogadro number, while Ω and V_m are the average atomic volume and molar volume of the FCC solid solution, respectively. The rate of vacancy generation due to σ-phase precipitation is then obtained by

$$\left(\frac{dc_{Va}^{ex}}{dt}\right)^{\sigma} = 2\pi RH|\varepsilon_r|N^{\sigma}\frac{\Omega}{\Omega_{Va}}G. \tag{13}$$

The governing equation that accounts for excess vacancy generation due to the σ-phase precipitation, their diffusion, and annihilation at available sinks (plane facets of the precipitates, residual dislocations, and grain boundaries) is simply

$$\frac{dc_{Va}^{ex}}{dt} = D_{Va}\nabla^2 c_{Va}^{ex} - c_{Va}^{ex} \times S + \left(\frac{dc_{Va}^{ex}}{dt}\right)^{\sigma} \tag{14}$$

where S represents the effective vacancy sink strength. A steady-state solution of Eq. (14) is well known from the irradiation theory [62,63] and allows to roughly estimate the corresponding concentration of the excess vacancies,

$$c_{Va}^{ex} \approx \frac{\left(\frac{dc_{Va}^{ex}}{dt}\right)^{\sigma}}{S} \approx \left(\frac{dc_{Va}^{ex}}{dt}\right)^{\sigma}\frac{L^2}{D_{Va}} \tag{15}$$

where L is the mean distance to the sinks. Introducing Eq. (15) into Eq. (9), we finally estimate the diffusion enhancement due to excess vacancies produced by the σ-phase precipitation,

$$\frac{D^{*\prime}}{D^*} = 1 + \frac{2\pi RH|\varepsilon_r|N^{\sigma}G}{D^*}L^2 = 1 + \frac{2f|\varepsilon_r|}{RD^*}GL^2 \tag{16}$$

where f is the volume fraction of σ-phase. Independent measurements of size of σ-phase precipitates after heat treatment at 1073 K revealed that their radius R and thickness H are within the ranges $\simeq 1$–4 μm and $\simeq 0.3-0.8$ μm, respectively, and their volume density $N^{\sigma} \simeq 5\times 10^{17} - 5\times 10^{16}$ m^3. Moreover, their growth rate G could be estimated to be $\simeq 10^{-11}$ m/s. Using the volume fraction of σ-phase $f = 0.27$ (Table 3) and $D^* \simeq 2\times 10^{-18} - 2\times 10^{-17}$ m^2/s for 1073 K (Fig. 9), simple estimates at 1073 K using the right part of Eq. (16) suggests that a diffusion enhancement by a factor of 2 to 11, consistent with our experimental values, is obtained if the mean distance to vacancy sinks $L = 10$ μm. This mean free path of vacancies seems reasonable, as it may correspond to the mean distance between dislocations in non-strained material (for a typical dislocation density of 10^{10} m^{-2}). It is worth noting however that L is an effective parameter of the model and may therefore account for additional vacancy sinks, such as interfaces and grain boundaries.

Eq. (16) allows as well a simple parameter check of the diffusion enhancement. Using its left part, one can see that for sub-micron precipitates, the diffusion enhancement is negligible, $D^{*\prime}/D^* \approx 1$. Micron-sized precipitates most efficiently produce vacancies. Later on, the vacancy production diminishes due to precipitate impingement and dominance of globular growth. In this latter case, most of the interfaces become incoherent, which provides a high density of sinks, where vacancies can annihilate. As a result, the excess vacancy concentration gets eliminated.

Eq. (15) approximates the point defect concentration at steady-state conditions. This approximation is very reasonable, since the precipitates do not grow significantly during the time needed to approach the stationary vacancy concentration, which can be estimated as $\tau_{Va} \approx \langle L\rangle^2/D_{Va} \approx 10^{-2}$ s at 1073 K. Since the vacancy generation term, $\left(dc_{Va}^{ex}/dt\right)^{\sigma}$, is in fact time-dependent, the vacancy supersaturation becomes time-dependent, too. Therefore, the averaged tracer diffusion coefficient, $\langle D^*\rangle$, determined experimentally is given by

$$\langle D^*\rangle = \int_0^t D^{*\prime}(\tau)d\tau, \tag{17}$$

where t is the diffusion time. Phase-field modeling may be used to refine the model and estimate the time-dependent diffusion acceleration. However, the time evolution of the vacancy excess (and of the corresponding diffusion enhancement) can be understood from Eq. (16).

The elaborated model correlates the specific volumetric effect related to the σ-phase precipitation with the measured diffusion enhancement. The impact of secondary phase formation on point defect concentration is well-known, e.g., in the case of oxidation, the atomic flux towards the oxide scale may involve a counterflow of vacancies into the substrate [64]. Moreover, the presence of non-equilibrium point defects (vacancies and self-interstitials) due to irradiation considerably affects the rate of diffusive phase transformations [65,66]. Our study provides further insights into the interrelation of atomic diffusion and diffusive phase transformation. Typically, equilibrium diffusion coefficients are used to model the secondary phase precipitations [22, 67]. We have found that non-equilibrium vacancies might be produced during precipitation. This affects the atomic diffusion rates, which in turn enhances the precipitation rates.

The interpretation of the observed diffusion enhancement remains tentative before a direct measurements of the vacancy concentration during precipitation, for example via positron annihilation spectroscopy. However, such measurements at 1073 K (about $0.67\,T_m$) are at least not straightforward, as equilibrium vacancy concentrations below 10^{-6} are expected [68]. The transient nature of the diffusion enhancement is a key characteristic, which significantly constrains the range of possible underlying mechanisms and the present analysis elucidates a transient generation of non-equilibrium vacancies is a most plausible one.

4.4. Impact of GB precipitates and a continuous network of precipitates within grains on short-circuit diffusion

The measured penetration profiles, Figs. 8 and 10, indicate a significant contribution of short-circuit diffusion in our experiments. In addition, we showed that the volume diffusion rates in the FCC solid solution and the σ-phase alloy are similar. This similarity greatly simplifies the interpretations. In particular, it implies that distinguishing between the matrix and the precipitates is not necessary for a correct extraction of the volume and short-circuit diffusion data from the penetration profiles. Consequently, well-known models for GB- or interphase boundary diffusion can be applied directly, without the need to develop specific frameworks. A proper analysis was required for a rigorous separation of the corresponding contribution of volume diffusion, as discussed in Section 4.2 using Eq. (1).

Depending on the temperature and the diffusion time, several microstructural features might potentially contribute to tracer penetration exceeding the typical depths for direct volume diffusion, i.e., greater than $5\sqrt{D_v t}$:

- stationary GBs (low- and high-angle GBs and/or special, low-Σ GBs);
- moving GBs;
- dislocations via pipe diffusion;
- interphase boundaries, i.e., diffusion along the FCC/σ (matrix/precipitate) boundaries;
- combination of different short-circuit pathways such as semi-coherent interphase boundaries with trailing misfit dislocations.

The shape of the penetration profile, i.e., the decay of the tracer concentration with the penetration depth, x, is characteristic of a given diffusion mechanism. Therefore, the latter is carefully analyzed in the following to elucidate the type and configuration of short circuits that contribute to diffusion.

Dislocation diffusion cannot explain the deep branches of the penetration profiles because the corresponding profiles must decay linearly with depth (contrary to the observed $6/5^{\text{th}}$ power dependence). Most importantly, the corresponding slope has to be time-independent [43], which is in strong contradiction to the results of the time-dependent diffusion measurements shown in Fig. 10.

Moving GBs can also be excluded since the σ-precipitates effectively pin GBs, and no "ghost" lines (seen in the case of moving GBs [69]) were found by a careful microstructure inspection. Again, the slopes of the penetration profiles are predicted to be time-independent [43], in disagreement with the present results.

Moving interphase boundaries. During the σ-phase precipitation, the allotriomorphs continuously thicken, resulting in a motion of the interphase boundaries. Following the theory developed for tracer diffusion along moving GBs [43], the motion of interphase boundaries would produce linear profiles against the penetration depth. Even though the diffusion profiles are nearly linear in Fig. 10, GB diffusion decays with the depth raised to the power of $6/5^{\text{th}}$, see Eq. (1). Since the short-circuit diffusion branches were measured over more than three orders of magnitude of decrease of the tracer concentration, a systematic curvature in the $\ln \bar{C}$-vs.-x coordinates is prominent. Thus, the motion of interphase boundaries does not explain the penetration profiles and can be ruled out.

We conclude that **stationary GBs** and/or **interface boundaries** (or their combination) dominate the deeper branches of the penetration profiles. This conclusion is further supported by a characteristic evolution of the penetration profiles measured at the same temperature for different diffusion times for the state HT-0, Fig. 10. Since about the same amount of the radioactive solution was applied to the sample surface, the residual activity remains almost unchanged, and the short-circuit branches progressively become shallower and shift to higher activities. This corresponds to an increasing amount of tracer atoms diffusing in the sample via short-circuits in the B-type kinetics regime, compare the profiles shown by black symbols in Fig. 10.

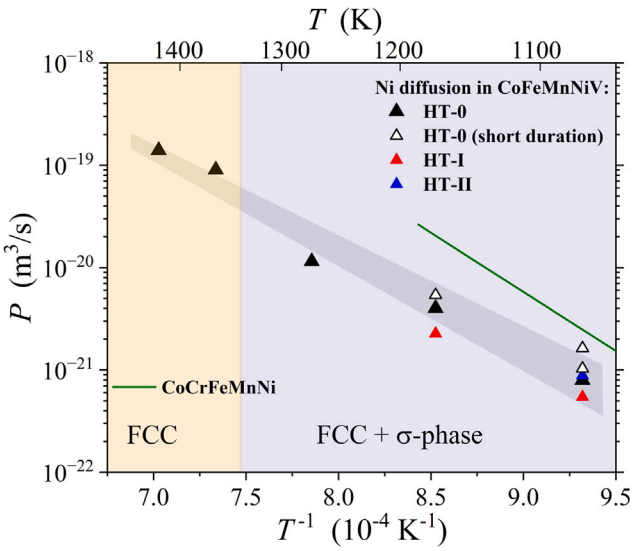

Fig. 15. Triple products determined for Ni GB diffusion in the HT-0 (black triangles), HT-I (red triangles) and HT-II states (blue triangle). The temperature intervals corresponding to single-phase (FCC solid solution) and two-phase (FCC+σ) equilibria are indicated by yellow and blue backgrounds, respectively. The shaded area corresponds to an Arrhenius approximation of the short-circuit diffusion rates in CoFeMnNiV alloy during σ-phase precipitation. For comparison, triple products for Ni GB diffusion in CoCrFeMnNi HEA [70] is shown with a green line.

Since the diffusivities in the low-angle GBs are significantly lower than those in the general high-angle GBs [39], the latter ones serve likely as the dominant paths for short-circuit diffusion. A large fraction of high-angle GBs is corroborated by the EBSD analysis, Fig. 3(a). These are general high-angle GBs which govern the deep tracer penetration at elevated temperatures corresponding to the single-phase FCC solid solution region. In Fig. 15, the determined triple products are presented as a function of the inverse absolute temperature.

Below about 1360 K, the GBs become progressively covered by σ-allotriomorphs. Nevertheless, the determined triple products follow roughly the same Arrhenius dependence indicated schematically by the shaded area in Fig. 15. We may deduce that the rates of GB diffusion, $P = s \cdot \delta \cdot D_{\text{gb}}$, in the FCC matrix are similar to the rates of interphase boundary (FCC/σ) diffusion, $P_{ipb} = s_{ipb} \cdot \delta_{ipb} \cdot D_{ipb}$. The GB diffusion experiments performed in precipitated microstructures, i.e., in the HT-I and HT-II states, are only slightly smaller than those determined by experiments for initial precipitate-free conditions. Even time-dependent measurements provide reproducibly similar short-circuit diffusion data, open and filled black triangles in Fig. 15.

Another argument supports the conclusion that interphase boundaries are important for short-circuit diffusion at lower temperatures. According to the GB diffusion theory [39,43], the ratio of the prefactors in Eq. (1), B/A, scales with the area density of the short-circuit paths. For example, in a polycrystalline material, $B/A \propto \delta/d$, where d is the grain size. A careful inspection of the penetration profiles in Fig. 10, indicates that the ratio B/A is larger by an order of magnitude for diffusion in the precipitated microstructures (HT-I and HT-II states) compared to those measured in the initial HT-0 state, especially for the short annealing times. We conclude that the density of short-circuits must increase dramatically in states HT-I and HT-II compared to HT-0. This increase correlates with the appearance of a nearly continuous network of σ-precipitates within grains after prolonged annealing treatments, see Figs. 4 and 5. From the perspective of interphase boundary diffusion, the formation of a precipitation network is equivalent to a

grain refinement from about 100 μm down to 5 to 10 μm, i.e., by a factor of 10, in excellent agreement with the diffusion experiments.

The analysis suggests that the diffusion rates for Ni atoms along the high-angle GBs within the FCC matrix and those along the FCC/σ interfaces are not very different. Indeed, the triple products P for Ni diffusion measured in the FCC alloy with pristine FCC/FCC boundaries, yellow shaded temperature interval in Fig. 15, turned out to be similar to those determined in the state with numerous σ-phase precipitations at the GBs, i.e. basically along the FCC/σ interfaces, the gray shaded area in Fig. 15. The similarity of the diffusion rates is supported by in fact unique Arrhenius-type temperature dependence for the whole dataset of the P values.

Spatially resolved isotope mapping was performed using the highly-enriched ^{64}Ni natural isotope and the ToF-SIMS analysis in order to distinguish the diffusion contributions of the general high-angle GBs within the FCC matrix and of the FCC/σ interphase boundaries. The applicability of this method has recently been demonstrated, e.g., for an eutectic high-entropy alloy [71]. However, due to relatively low intensities of the recorded ^{64}Ni signal and a corresponding large scatter of the data points, no noteworthy contrast between the GB (FCC/FCC interfaces) and IPB (FCC/σ) diffusion behaviors was observed, making a quantitative separation of the respective contributions difficult. However, this results supports indirectly our conclusion that the diffusion properties of the high-angle GBs within the FCC matrix are similar to those of the FCC/σ interphase boundaries.

In Fig. 15, the triple products of Ni diffusion in CoFeMnNiV are compared with those measured in CoCrFeMnNi by Vaidya et al. [70], see green line. While bulk diffusion of Ni is retarded in CoCrFeMnNi with respect to that in CoFeMnNiV, a reverse relation is clear for GB and interphase boundary diffusion in these alloys. The atomistic reasons of this phenomenon have still to be elucidated as well as a detailed understanding of the FCC/σ interphase structure. For example, recent ab-initio studies on the FCC/σ interfaces in comparatively simpler Fe–Cr system [72] have already demonstrated the complexity associated with describing the atomic and energetic characteristics of such interfaces. In compositionally complex high-entropy alloys, the additional chemical disorder and local compositional variations at the interface [73] result in specific structure–property relations influencing, e.g., the interface diffusion rates [74].

5. Summary and conclusions

Ni diffusion in an equiatomic CoFeMnNiV high-entropy alloy, which is prone to σ-phase precipitation at moderate temperatures, is measured in an extended temperature interval covering both single-phase (FCC solid solution) and two-phase (FCC + σ) regions. The measurements are accompanied by Ni diffusion measurements in a bulk σ-phase alloy, which was synthesized with the composition of the σ-precipitates determined by SEM/EDS. The following main conclusions can be formulated:

- Replacing Cr in the equiatomic Cantor alloy by V to form the CoFeMnNiV alloy leads to a dramatic enhancement of σ-phase precipitation. This shows that V stabilizes the σ-phase more effectively than Cr.
- When the alloys are single-phase FCC, the Ni bulk diffusion coefficient measured at a given temperature in the CoFeMnNiV alloy is larger within a factor of two to three than that in the Cantor alloy. This enhancement correlates with increased lattice distortions by V substitution of Cr as it was discussed by Zhang et al. [34].
- The Ni diffusion rates in the equiatomic CoFeMnNiV HEA and the corresponding bulk σ-phase alloy are found to be comparable. This finding resembles that observed previously in the Co–Cr–Fe–Mn–Ni system [51].
- In CoFeMnNiV, at temperatures below 1338 K, σ-phase precipitation occurs. The bulk Ni diffusion rates measured in these conditions exceed those predicted by a linear Arrhenius-type extrapolation of the high-temperature data. A similar kink in the Arrhenius plot was also reported previously for the Cantor alloy [52].
- This relative diffusion enhancement in CoFeMnNiV is interpreted in terms of the generation of non-equilibrium vacancies during precipitation of the σ-phase. The conclusion is corroborated by the time-dependence diffusion measurements at 1173 K and 1073 K. At 1173 K, the Ni bulk diffusion coefficient in a preliminary equilibrated microstructure (HT-I state) agrees nicely with the extrapolation of the high-temperature diffusion data.
- Time-dependent measurements at 1073 K even in equilibrated microstructure yield the Ni diffusion coefficients enhanced with respect to the Arrhenius dependence elaborated from high-temperature experiments.
- A short-circuit diffusion contribution is consistently observed for Ni diffusion in the CoFeMnNiV alloy, especially at low temperatures. At the same absolute temperatures, short-circuit diffusion of Ni in CoCrFeMnNi is found to be faster than that in CoFeMnNiV, whereas a reverse relationship holds for the corresponding bulk diffusivities.
- The short-circuit diffusion contribution in CoFeMnNiV is interpreted in terms of both grain boundary and interphase boundary (FCC/σ) diffusion, which are found to feature similar rates.

The present work shows that the precipitation of TCP phases like σ can influence the bulk diffusion rates in the matrix. Depending on the volumetric effect by precipitation and potentially on the coherency relations, the diffusion rates in the matrix might significantly be enhanced, giving rise to strong coupling of the transformation and diffusion rates.

CRediT authorship contribution statement

Aditya Burla: Writing – original draft, Visualization, Methodology, Investigation, Formal analysis, Data curation. **Aditya Srinivasan Tirunilai:** Writing – original draft, Visualization, Methodology, Investigation, Formal analysis, Data curation. **Mathias Redondo Garcia:** Writing – original draft, Visualization, Methodology, Investigation, Formal analysis. **G. Mohan Muralikrishna:** Writing – review & editing, Methodology, Investigation, Conceptualization. **Vladimir A. Esin:** Writing – review & editing, Visualization, Validation, Formal analysis, Data curation. **Daniel Schliephake:** Methodology, Investigation. **Alexander Kauffmann:** Writing – review & editing, Project administration. **Gerhard Wilde:** Writing – review & editing, Validation, Supervision, Resources, Project administration. **Guillaume Laplanche:** Writing – review & editing, Visualization, Validation, Supervision, Resources, Project administration, Funding acquisition, Conceptualization. **Sergiy V. Divinski:** Writing – review & editing, Visualization, Validation, Supervision, Resources, Project administration, Funding acquisition, Conceptualization.

Declaration of competing interest

The authors declare that they have no known competing financial interests or personal relationships that could have appeared to influence the work reported in this paper.

Acknowledgments

This work was supported by the German Research Foundation, projects DI 1419/24-1 (project number 509804947), SR 170/2-1 (project number 553555345), and LA 3607/6-1 (project number 564857507).

Appendix A. Supplementary data

Supplementary material related to this article can be found online at https://doi.org/10.1016/j.actamat.2026.122543.

References

[1] J. Yeh, S. Chen, S. Lin, J. Gan, T. Chin, T. Shun, C. Tsau, S. Chang, Nanostructured high-entropy alloys with multiple principal elements: Novel alloy design concepts and outcomes, Adv. Eng. Mater. 6 (2004) 299.

[2] B. Cantor, I. Chang, P. Knight, A. Vincent, Microstructural development in equiatomic multicomponent alloys, Mater. Sci. Eng.: A 375–377 (2004) 213.

[3] D. Miracle, O. Senkov, A critical review of high entropy alloys and related concepts, Acta Mater. 122 (2017) 448.

[4] B. Gludovatz, A. Hohenwarter, D. Catoor, E.H. Chang, E.P. George, R.O. Ritchie, A fracture-resistant high-entropy alloy for cryogenic applications, Science 345 (2014) 1153.

[5] B. Bian, N. Guo, H. Yang, R. Guo, L. Yang, Y. Wu, J. Qiao, A novel cobalt-free FeMnCrNi medium-entropy alloy with exceptional yield strength and ductility at cryogenic temperature, J. Alloys Compd. 827 (2020) 153981.

[6] P. Sathiyamoorthi, J. Moon, J.W. Bae, P. Asghari-Rad, H.S. Kim, Superior cryogenic tensile properties of ultrafine-grained CoCrNi medium-entropy alloy produced by high-pressure torsion and annealing, Scr. Mater. 163 (2019) 152.

[7] F. Otto, A. Dlouhý, C. Somsen, H. Bei, G. Eggeler, E. George, The influences of temperature and microstructure on the tensile properties of a CoCrFeMnNi high-entropy alloy, Acta Mater. 61 (2013) 5743.

[8] G. Laplanche, A. Kostka, C. Reinhart, J. Hunfeld, G. Eggeler, E. George, Reasons for the superior mechanical properties of medium-entropy CrCoNi compared to high-entropy CrMnFeCoNi, Acta Mater. 128 (2017) 292.

[9] K. Lu, A. Chauhan, A.S. Tirunilai, J. Freudenberger, A. Kauffmann, M. Heilmaier, J. Aktaa, Deformation mechanisms of CoCrFeMnNi high-entropy alloy under low-cycle-fatigue loading, Acta Mater. 215 (2021) 117089.

[10] B. Schuh, F. Mendez-Martin, B. Völker, E. George, H. Clemens, R. Pippan, A. Hohenwarter, Mechanical properties, microstructure and thermal stability of a nanocrystalline CoCrFeMnNi high-entropy alloy after severe plastic deformation, Acta Mater. 96 (2015) 258.

[11] F. Otto, A. Dlouhý, K. Pradeep, M. Kuběnová, D. Raabe, G. Eggeler, E. George, Decomposition of the single-phase high-entropy alloy CrMnFeCoNi after prolonged anneals at intermediate temperatures, Acta Mater. 112 (2016) 40.

[12] T. Storch, M.R. Garcia, A.S. Tirunilai, C. Somsen, Y. Li, J. Kiese, G. Laplanche, Phase stability and sigma (σ)-phase precipitation kinetics in a new wrought CrCoNi-based medium-entropy superalloy, Acta Mater. 300 (2025) 121479.

[13] G. Cheng, Y. Shi, Y. Wang, F. Zhang, R. Li, Y. Zhou, Z. Wu, C. Ma, Z. Lei, Z. Lu, Enhancing strengthening effect of topologically close-packed superlattices in medium-entropy alloys via enabling imperfect atomic packing, Acta Mater. 271 (2024) 119903.

[14] C. Rae, R. Reed, The precipitation of topologically close-packed phases in rhenium-containing superalloys, Acta Mater. 49 (2001) 4113.

[15] R. Reed, D. Cox, C. Rae, Damage accumulation during creep deformation of a single crystal superalloy at 1150°C, Mater. Sci. Eng.: A 448 (2007) 121479.

[16] A.S. Tirunilai, A. Wolf, G. Laplanche, Effect of TCP phases on tensile properties of engineering alloys: Insights gained from a CrMnFeCoNi high-entropy alloy, Acta Mater. 301 (2025) 121530.

[17] T. Storch, J. Hunfeld, Y. Li, J. Kiese, D. Petrell, J.-M. Joubert, G. Eggeler, G. Laplanche, Optimizing creep resistance in wrought superalloys: Effect of small variations in Ti and Al content on γ' and σ-phase precipitation kinetics, Met. Mater. Trans. A (2026) 1.

[18] Z. Wu, H. Bei, F. Otto, G. Pharr, E. George, Recovery, recrystallization, grain growth and phase stability of a family of FCC-structured multi-component equiatomic solid solution alloys, Intermetallics 46 (2014) 131.

[19] Z. Wu, H. Bei, G. Pharr, E. George, Temperature dependence of the mechanical properties of equiatomic solid solution alloys with face-centered cubic crystal structures, Acta Mater. 81 (2014) 428.

[20] B. Yin, F. Maresca, W. Curtin, Vanadium is an optimal element for strengthening in both FCC and BCC high-entropy alloys, Acta Mater. 188 (2020) 486.

[21] A. Tirunilai, C. Somsen, G. Laplanche, Excellent strength-ductility combination in the absence of twinning in a novel single-phase VMnFeCoNi high-entropy alloy, Scr. Mater. 256 (2025) 116430.

[22] G. Laplanche, S. Berglund, C. Reinhart, A. Kostka, F. Fox, E. George, Phase stability and kinetics of σ-phase precipitation in CrMnFeCoNi high-entropy alloys, Acta Mater. 161 (2018) 338.

[23] A.S. Tirunilai, Z. Ayrildi, B. Şen, M. Rajkowski, M.R. Garcia, M. Stricker, G. Laplanche, Microstructure evolution of a VMnFeCoNi high-entropy alloy after synthesis, swaging and annealing, Adv. Eng. Mater. (2026).

[24] T. Koyama, Y. Tsukada, T. Abe, Simple approach for evaluating the possibility of sluggish diffusion in high-entropy alloys, J. Phase Equilib. Diffus. 43 (2022) 68.

[25] M. Vaidya, S. Trubel, B. Murty, G. Wilde, S.V. Divinski, Ni tracer diffusion in CoCrFeNi and CoCrFeMnNi high entropy alloys, J. Alloys Compd. 688 (2016) 994.

[26] M. Vaidya, K. Pradeep, B. Murty, G. Wilde, S.V. Divinski, Bulk tracer diffusion in CoCrFeNi and CoCrFeMnNi high entropy alloys, Acta Mater. 146 (2018) 211.

[27] A. Durand, L. Peng, G. Laplanche, J. Morris, E. George, G. Eggeler, Interdiffusion in Cr–Fe–Co–Ni medium-entropy alloys, Intermetallics 122 (2020) 106789.

[28] J. Kottke, D. Utt, M. Laurent-Brocq, A. Fareed, D. Gaertner, L. Perriere, L. Rogal, A. Stukowski, K. Albe, S.V. Divinski, G. Wilde, Experimental and theoretical study of tracer diffusion in a series of $(CoCrFeMn)_{100-x}Ni_x$ alloys, Acta Mater. 194 (2020) 236.

[29] M. Rajkowski, A. Durand, J.R. Morris, G. Eggeler, G. Laplanche, High-throughput approach for investigating interdiffusion in medium- and high-entropy alloys, J. Appl. Phys. 135 (2024) 175101.

[30] K.Y. Tsai, M.H. Tsai, J.W. Yeh, Sluggish diffusion in Co–Cr–Fe–Mn–Ni high-entropy alloys, Acta Mater. 61 (2013) 4887.

[31] A. Dash, A. Paul, S. Sen, S.V. Divinski, J. Kundin, I. Steinbach, B. Grabowski, X. Zhang, Recent advances in understanding diffusion in multiprincipal element systems, Annu. Rev. Mater. Res. 52 (2022) 383.

[32] S. Sen, X. Zhang, L. Rogal, G. Wilde, B. Grabowski, S.V. Divinski, 'Anti-sluggish' Ti diffusion in HCP high-entropy alloys: Chemical complexity vs. lattice distortions, Scr. Mater. 224 (2023) 115117.

[33] J. Zhang, C. Gadelmeier, S. Sen, R. Wang, X. Zhang, Y. Zhong, U. Glatzel, B. Grabowski, G. Wilde, S.V. Divinski, Zr diffusion in BCC refractory high entropy alloys: A case of 'non-sluggish' diffusion behavior, Acta Mater. 233 (2022) 117970.

[34] J. Zhang, X. Xu, F. Körmann, W. Yin, X. Zhang, C. Gadelmeier, U. Glatzel, B. Grabowski, R. Li, G. Liu, B. Wang, G. Wilde, S.V. Divinski, Lattice distortions and non-sluggish diffusion in BCC refractory high entropy alloys, Acta Mater. 297 (2025) 121283.

[35] G. Laplanche, O. Horst, F. Otto, G. Eggeler, E. George, Microstructural evolution of a CoCrFeMnNi high-entropy alloy after swaging and annealing, J. Alloys Compd. 647 (2015) 548.

[36] K. Kishida, M. Okutani, H. Suzuki, H. Inui, M. Heilmaier, D. Raabe, Room-temperature deformation of single crystals of the sigma-phase compound FeCr with the tetragonal D8b structure investigated by micropillar compression, Acta Mater. 249 (2023) 118829.

[37] J.-M. Joubert, Y. Kalchev, A. Fantin, J.-C. Crivello, R. Zehl, E. Elkaim, G. Laplanche, Site occupancies in a chemically complex σ-phase from the high-entropy Cr–Mn–Fe–Co–Ni system, Acta Mater. 259 (2023) 119277.

[38] D. Porter, K. Easterling, Phase Transformations in Metals and Alloys (Revised Reprint), CRC Press, 2009.

[39] A. Paul, T. Laurila, V. Vuorinen, S. Divinski, Thermodynamics, Diffusion and the Kirkendall Effect in Solids, Springer, 2014.

[40] L. Harrison, Influence of dislocations on diffusion kinetics in solids with particular reference to the alkali halides, Trans. Faraday Soc. 57 (1961) 1191.

[41] A. Le Claire, The analysis of grain boundary diffusion measurements, Br. J. Appl. Phys. 14 (1963) 351.

[42] T. Suzuoka, Exact solutions of two ideal cases in grain boundary diffusion problem and the application to sectioning method, J. Phys. Soc. Japan 19 (1964) 839.

[43] I. Kaur, Y. Mishin, W. Gust, Fundamentals of Grain and Interface Boundary Diffusion, Wiley & Sons LTD, 1995.

[44] Y. Amouyal, S. Divinski, Y. Estrin, E. Rabkin, Short-circuit diffusion in an ultrafine-grained copper–zirconium alloy produced by equal channel angular pressing, Acta Mater. 55 (2007) 5968.

[45] H. Mehrer, Diffusion in Solids: Fundamentals, Methods, Materials, Diffusion-Controlled Processes, Springer, Berlin, Heidelberg, 2007.

[46] E. Hart, On the role of dislocations in bulk diffusion, Acta Metall. 5 (1957) 597.

[47] J. Garnett, XII. Colours in metal glasses and in metallic films, Philos. Trans. R. Soc. Lond. Ser. A 203 (1904) 385.

[48] J. Kalnin, E. Kotomin, J. Maier, Calculations of the effective diffusion coefficient for inhomogeneous media, J. Phys. Chem. Solids 63 (2002) 449.

[49] R. Li, B. Bian, G. Wilde, Y. Zhang, S. Divinski, Bulk and grain boundary tracer diffusion in multiphase $AlCoCrFeNiTi_{0.2}$ compositionally complex alloy, Acta Mater. 261 (2023) 119352.

[50] D. Gaertner, L. Belkacemi, V.A. Esin, F. Jomard, A.A. Fedotov, J. Schell, J.V. Osinskaya, A.V. Pokoev, C. Duhamel, A. Paul, S.V. Divinski, Techniques of tracer diffusion measurements in metals, alloys and compounds, Diffus. Found. 29 (2021) 31.

[51] J. Zhang, G.M. Muralikrishna, A. Asabre, Y. Kalchev, J. Müller, B. Butz, S. Hilke, H. Rösner, G. Laplanche, S.V. Divinski, G. Wilde, Tracer diffusion in the σ phase of the cocrfemnni system, Acta Mater. 203 (2021) 116498.

[52] D. Gaertner, J. Kottke, Y. Chumlyakov, F. Hergemöller, G. Wilde, S. Divinski, Tracer diffusion in single crystalline CoCrFeNi and CoCrFeMnNi high-entropy alloys: Kinetic hints towards a low-temperature phase instability of the solid-solution? Scr. Mater. 187 (2020) 57.

[53] A. Smekhova, D. Gaertner, A. Kuzmin, A. Guilherme-Buzanich, G. Schuck, I. Zizak, G. Wilde, K. Yusenko, S. Divinski, Anomalies in the short-range local environment and atomic diffusion in single crystalline equiatomic CrMnFeCoNi high-entropy alloy, Nano Res. 17 (2024) 5336.

[54] S. Nenno, M. Tagaya, Z. Nishiyama, Orientation relationships between gamma (f.c.c.) and sigma phases in an Iron-Chromium-Nickel alloy, Trans. Japan Inst. Met. 3 (1962) 82.
[55] D. Gaertner, K. Abrahams, J. Kottke, V. Esin, I. Steinbach, G. Wilde, S. Divinski, Concentration-dependent atomic mobilities in FCC CoCrFeMnNi high-entropy alloys, Acta Mater. 166 (2019) 357.
[56] D. Gaertner, J. Kundin, N. Esakkiraja, J. Berndt, A. Durand, J. Kottke, S. Klemme, G. Laplanche, G. Eggeler, G. Wilde, A. Paul, I. Steinbach, S. Divinski, Tracer diffusion under a concentration gradient: A pathway for a consistent development of mobility databases in multicomponent alloys, J. Alloys Compd. 930 (2023) 167301.
[57] J. Rickman, Tracer diffusion in the presence of segregating obstacles, Physica A 390 (2011) 456.
[58] Y. Wu, F. Zhang, X. Yuan, H. Huang, X. Wen, Y. Wang, M. Zhang, H. Wu, X. Liu, H. Wang, S. Jiang, Z. Lu, Short-range ordering and its effects on mechanical properties of high-entropy alloys, J. Mater. Sci. Technol. 62 (2021) 214.
[59] Y. Li, T. Colnaghi, Y. Gong, H. Zhang, Y. Yu, Y. Wei, B. Gan, M. Song, A. Marek, M. Rampp, S. Zhang, Z. Pei, M. Wuttig, S. Ghosh, F. Körmann, J. Neugebauer, Z. Wang, B. Gault, Machine learning-enabled tomographic imaging of chemical short-range atomic ordering, Adv. Mater. 36 (2024) 2407564, https://advanced.onlinelibrary.wiley.com/doi/pdf/10.1002/adma.202407564.
[60] N. Stolwijk, Correlation factors for diffusion in binary alloys with short-range order, Phys. Status Solidi (B) 105 (1981) 223, https://onlinelibrary.wiley.com/doi/pdf/10.1002/pssb.2221050124.
[61] K. Li, T. Schuler, C.-C. Fu, M. Nastar, Vacancy formation free energy in concentrated alloys: Equilibrium vs. random sampling, Acta Mater. 281 (2024) 120355.
[62] M. Kiritani, H. Takata, Dynamic studies of defect mobility using high voltage electron microscopy, J. Nucl. Mater. 69–70 (1978) 277.
[63] K. Gurov, A. Tsepelev, The kinetics of radiation point defect accumulation in metals during irradiation, J. Nucl. Mater. 182 (1991) 240.
[64] J. Harris, Vacancy injection during oxidation – A re-examination of the evidence, Acta Metall. 26 (1978) 1033.
[65] M. Nastar, L. Belkacemi, E. Meslin, M. Loyer-Prost, Thermodynamic model for lattice point defect-mediated semi-coherent precipitation in alloys, Nat. Commun. Mater. 2 (2021) 32.
[66] F. Soisson, M. Nastar, Atomistic simulations of diffusive phase transformations with non-conservative point defects, MRS Commun. 12 (2022) 1015.
[67] J. Christian, The Theory of Transformations in Metals and Alloys, Pergamon, Oxford, 2002.
[68] L. Xu, Y.-J. Wang, Y.-F. Guo, S. Ogata, Entropy-biased vacancy equilibria in multi-principal-element alloys, Scr. Mater. 282 (2026) 117397.
[69] S. Divinski, M. Lohmann, T. Surholt, C. Herzig, Grain boundary motion during Ag and Cu grain boundary diffusion in Cu Polycrystals, Interface Sci. 9 (2001) 357.
[70] M. Vaidya, K. Pradeep, B. Murty, G. Wilde, S. Divinski, Radioactive isotopes reveal a non sluggish kinetics of grain boundary diffusion in high entropy alloys, Sci. Rep. 7 (2017) 1.
[71] H. Zhang, G.M. Muralikrishna, A. Akbari, H. Rösner, B.J. Tyler, S. Divinski, G. Wilde, Grain- and interphase boundary diffusion in eutectic alcocrfeni2.1 compositionally complex alloy, Acta Mater. 294 (2025).
[72] S. San, Y. Wang, J. Yu, M.V. Glazoff, M.C. Gao, Ab initio prediction of FeCr sigma (001)/FCC Fe(111) interfacial energy: Effect of interfacial doping of C, B, and N, Phys. Rev. Mater. 9 (2025) 053602.
[73] J. Luo, N. Zhou, High-entropy grain boundaries, Commun. Mater. 4 (2023) 7.
[74] B. Yadav, G.M. Muralikrishna, M. Vaidya, G. Wilde, S. Divinski, Grain boundary diffusion in compositionally complex alloys: A comprehensive review, Int. Mater. Rev. 71 (2026) 129.